University of Dundee

MASTER OF PHILOSOPHY

Computer-assisted colour fundus image analysis

Chin, Khai Sing

Award date:
2011

Awarding institution:
University of Dundee

MASTER OF PHILOSOPHY

Computer-assisted colour fundus image analysis

Khai Sing Chin

2011

University of Dundee

Computer-Assisted Colour Fundus Image Analysis

A thesis submitted in application for the degree of Master of Philosophy

Khai Sing Chin

School of Computing

University of Dundee

February 2011

CONTENTS

ACKNOWLEDGEMENTS

First of all, I would like to thank my supervisor, Prof Emanuele Trucco who had provided me with the opportunity to work in this project with his team. I would like to express my appreciation for his guidance and patience throughout my research.

A big thank you to all my colleagues who have helped me tremendously with their technical expertise and helpful advice: Adria, Jerry, Vijay, Roy, Kris, Sebastian. They had been wonderful colleagues and friends.

I would also like to thank Dr. Alex Doney for procuring the Ninewells screening images under a TENOVUS grant and Prof Ian Deary for access to a sample of the Lothian Birth Cohort 1936 images. Special thanks also to Dr. Peter Wilson and Dr. Lai Ling Tan for their clinical input and useful discussions.

Finally to my family for their endless support and last but not least, to How Run who is ever encouraging and is always by my side through thick and thin.

SUMMARY OF CANDIDATE'S ACTIVITIES

This work has been reported in the following research papers.

K.S Chin, E.Trucco, "Fovea Detection Using Anatomical Priors and Vessel Density", *Opthalmic Image Analysis Workshop, Liverpool*, December 2011.

A.Giachetti, K.S Chin, E.Trucco, C. Cobb, P. J Wilson, "Multiresolution localization and segmentation of the optical disc in Fundus images using inpainted background and vessel information", *Proc. 18th IEEE Intl Conf on Image Processing, Brussels,* Sep 2011.

A.P. Rovira, T.MacGillivray, E Trucco, K S Chin, K Zutis, C Lupascu, D Tegolo, A Giachetti, PJ Wilson, A Doney, B Dhillon: "VAMPIRE: Vessel Assessment and Measurement Platform for Images of the Retina", *Proc IEEE Int Symp on Engineering in Biology and Medicine, Boston,* Aug-Sep 2011.

The MPhil work was part of a multidisciplinary study involving the VAMPIRE team and the Diabetes Research Centre (Dr Alex Doney) and funded by TENOVUS.

The author has attended the International Summer School on Pattern Recognition (ISSPR) in Plymouth, July 2010, organized by Loughborough University.

The author has also co-organized the UK PhD Computer Vision Student Workshop 2011, a satellite workshop of BMVC 2011, and the annual PhD Students Symposium of the School of Computing, 2011.

LIST OF FIGURES

LIST OF TABLES

ABSTRACT

Research in automatic retina image analysis has become increasingly important in ophthalmology. The retina is the only location where blood vessels can be directly visualized non-invasively in vivo. Hence, it serves as a 'window' to some of the pathologies like glaucoma, cerebrovascular and cardiovascular complications. Any change in the optic disc structure, blood vessel width, blood vessel tortuosity, and presence of lesion serves as indications of the pathologies. Realizing the importance of retina image analysis in pathology detection, there has been increasing research in ophthalmology to find statistical proof of correlation between certain retinal features with certain types of pathologies. Automatic retina image analysis can play an important part in the processing of large number of data required in correlational studies. It also provides a more qualitative and standardized assessment of retinal images which is harder to achieve in direct ophthalmoscopy.

In this thesis we present two automatic retinal image analysis algorithms; fovea detection and artery-vein classification. The fovea, which lies within the macula region, is responsible for high resolution vision. Hence, presence of lesions or changes in the morphology of this region may be signs of pathologies such as age-related macular disease, which can cause blindness. Automatic detection of fovea allows automatic analysis of this region for the identification of macular related diseases. Our detection framework models the fovea region as an avascular region coupled with prior anatomical information on the fovea position in the retina. The artery-vein classification algorithm aims to classify vessels for the purpose of automating the estimation of artery-vein ratio (AVR). Numerous researches have shown that AVR is a well-established indicator of cardiovascular diseases. Automated estimation of AVR is an important step to process large number of images, for diagnosis as well as for correlational studies.

DECLARATION BY THE AUTHOR

I hereby declare that I am the author of this thesis; that all references cited have been consulted by me; that the work of which this thesis is a record has been done by me, and that it has not been previously accepted for a higher degree.

Signed

Khai Sing Chin

February 2012

CHAPTER 1

INTRODUCTION

1.1 About this chapter

This chapter presents an overview of the research in this thesis, mainly its objective, motivation and finally, the structure of this thesis. All experiments in this thesis are done in MATLAB©.

1.2 Objective

The objective of this thesis is:

I. To develop efficient automatic retinal image analysis tools to aid clinical diagnosis as well as to allow a more efficient and low-cost large image data processing for correlational studies.

II. To refine and expand the current retina analysis tool previously developed in our group, VAMPIRE [1].

1.3 Motivation

Direct ophthalmoscopy is subjective and may vary with doctors. Automatic algorithm-driven measurements using fundus photography will increase repeatability, and is more standardized. Moreover, taking manual measurements from retinal fundus images is time consuming and obviously not ideal for the analysis of large image datasets. Hence, there is an increasing need for a reliable automatic pathology detection and classification of the retina.

In this thesis, we present two automated retinal image processing algorithms: fovea detection and artery-vein classification. Fovea is the region in the retina responsible for central photopic and high-resolution vision [26]. Therefore any abnormal changes to this region may lead to serious vision loss or even blindness. Various diseases are

related to this region, for example, age related macular degeneration (AMD) and macular oedema.

AMD is a disease characterized by yellowish lesions, found in both macula-fovea region and peripheral retina [26] whereas macular oedema is a vision threatening complication of diabetic retinopathy which is recognized by the presence of exudates in the macula-fovea region [108]. Therefore, detection of the fovea is important in order to automate the analysis for macula-related diseases. Besides, fovea detection is crucial to set up fundus coordinate systems, in which the horizontal axis goes through the optic disc and the fovea. Such coordinate systems are important to characterize the spatial distribution of lesions, such as the grading of diabetic retinopathy. Numerous work has been done to detect this region in color fundus images [18, 19, 20, 21, 23, 24, 25]. The main challenge in detecting macula-fovea detection is wide variation of its appearance due to pathologies. Several authors have also attempted to detect this region based on its relative position to the optic disc using a fixed ratio, disc-to-macula distance to disc-diameter ratio (DM:DD). However, this ratio is dependent on the size of optic disc and cannot be regarded as a constant. This is because optic disc size varies even in healthy people. Research has shown significant variation in optic disc size in people of different race [109, 110] and gender [109]. In people with retina pathologies, the variation in optic disc size is even larger [28, 30]. We developed our fovea detection algorithm aiming to address these problems. The method and its results are presented in Chapter 3.
The second automated retina image processing algorithm we present in this thesis is the artery-vein classification. This algorithm was developed to automate arterio-venous ratio (AVR) estimation. The arterio-venous ratio (AVR) is a medical measurement that is often used to quantify generalized retinal arteriolar narrowing [47] and has been found to have a link with hypertension, risk of diabetes mellitus, risk of coronary heart disease and cerebral atrophy [78, 79, 80, 8]. Computer-assisted estimation of AVR is

necessary because retinal arteriolar narrowing is difficult to quantify objectively through direct ophthalmoscopy and manual estimation. Research has also shown direct ophthalmology to be subjective especially in the detection of subtle retinal vascular changes [47, 69, 71]. Numerous semi-automated systems [104, 105] and automated systems [8, 10, 11, 106] have been developed for AVR estimation to aid in clinical research of the relation of AVR with different pathologies. The main challenge in developing a fully automated AVR estimation system is artery-vein classification. The challenge in artery-vein classification is the lack of an absolute definition for the appearance of artery and vein. Although artery is often defined as being brighter, having stronger central reflex and thinner compared to vein, it is only true when compared to its surrounding vessels. Hence, global classification using these vessel appearance features will pose problem. Several authors have also attempted to use vessel structure information to classify vessels into artery and vein. However, it is heavily dependent on the quality of vessel segmentation. In this thesis, we attempted to solve the problem of artery-vein classification. The method and its result are presented in Chapter 5.

1.4 Data set

In this thesis, all algorithms were run on images from the TENOVUS dataset. TENOVUS is a data set of 1,168 color fundus images which are part of Tayside diabetic screening programme at Ninewells Hospital, Dundee, in accordance to the current regulations (ethics, Caldicott, anonymization). The images were captured with different cameras at a similar FOV (field-of-view) around 40°-45°. The resolution ranges from 760x570, 1728x1152, to 3504x2336, the later ones acquired with a Canon EOS 20D and stored as JPEG. They are currently being used in a study to derive retinal biomarkers for cardio-vasculature diseases.

1.5 Structure of thesis

In Chapter 1, an overview of the research is presented along with the aim and motivation of this thesis. The remainder of this thesis is structured as follows.

- **Chapter 2: Clinical background and motivation**

  This chapter introduces the retina, different types of retinal image screening as well as the clinical motivation behind retinal image analysis. There is also a brief discussion on the importance of automated retina image analysis system and finally an introduction on our group's automated retinal analysis software, VAMPIRE.

- **Chapter 3: Fovea detection**

  In this chapter, we introduce a retinal landmark detection algorithm we developed, fovea detection, which is an important feature for pathology diagnosis. In our algorithm, we utilize prior anatomical information to identify the region where fovea is positioned in the retina. To locate the center of the fovea region, we model it as the center of an avascular region. We test the algorithm and the result is discussed.

- **Chapter 4: Interface tool for AVR estimation**

  In this chapter, we introduce a framework for artery-vein ratio (AVR) estimation. It combines manual user input using an interface tool and as well as automatic computation of branching coefficients and vessel width from the automated retinal analysis software developed in our group, VAMPIRE. The steps and method for AVR calculation are also presented.

- **Chapter 5: Automatic artery-vein classification**

  In this chapter, we propose a method for automatic artery-vein classification in an effort to automate the manual user input stage for AVR calculation which we discuss in Chapter 4. Our classification method aims to avoid using vessel

appearance globally due to the variation of vessel appearance within the same image as well as across different images. Hence, we propose local classification by comparing each vessel's intensity value to its nearest neighboring vessel. An initial test of the algorithm was performed and its result discussed in this chapter.

- **Chapter 6: Conclusion and future work**

  Finally, this chapter summarizes the work done in this thesis, and proposes possible future work.

CHAPTER 2

CLINICAL BACKGROUND AND MOTIVATION

2.1 About this chapter

This chapter gives a brief introduction on the anatomical structure of the retina in Section 2.2 and discusses about the types of information that can be obtained from the retina in Section 2.3. In Section 2.4, we discuss the different types of retinal image screening as well as the motivation behind retinal image analysis. We also look at the importance of automated retina image analysis system in Section 2.5 and finally introduce our group's automated retinal analysis software, VAMPIRE, in Section 2.6.

2.2 The retina

Retina is the sensory layer of the eye. It contains photosensitive cells which convert incident light into signals which is then carried to the brain by the optic nerve. The brain then processes the signal and which finally allows us to 'see' and interpret the object in front of our eyes. The retina contains three important components; optic disc (or optic nerve head), macula, and vasculature.

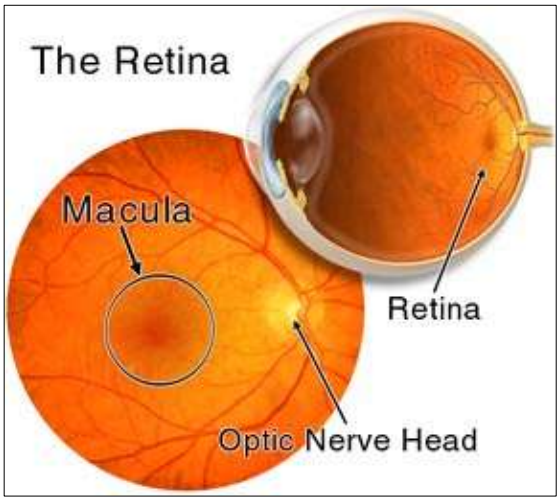

Figure 2.1: Structure of the eye – the retina is a light sensitive layer at the back of the eye where light is received and transformed into nerve impulse which is then sent to the brain through optic nerve. (Source: St Luke's cataract and laser institute)

The optic disc is responsible for transferring signal from retina to the brain to be interpreted. Optic disc abnormalities could be a marker for several diseases such as glaucoma and astigmatism [88]. In the middle of the macula is the fovea which is responsible for central photopic and high resolution vision [26]. Because of this, any abnormality occurring within this region may lead to blindness. The vasculature is not only responsible for supplying blood to the retina, it also shares similar anatomical and physiological characteristics with the cerebral and coronary circulations [47]. Therefore, changes in other parts of the body will affect the vasculature in retina. The vasculature in the retina has the advantage that it can be viewed by direct ophthalmoscopy or through digital retinal imaging. Current research in automated retinal analysis is targeted in detecting these landmarks to aid in diagnosis. Automated detection of the landmarks are also important to establish a retinal reference coordinate system before systems can proceed to perform analysis of identifying pathology entity as well as to enable mapping of lesion distribution. In the next section, we will elaborate further on the information that can be extracted from retinal images to aid in clinical diagnosis.

2.3 What the retina can tell us

2.3.1 Retinal Pathologies

Figure 2.2: Left: Healthy retina image (Source: MESSIDOR [49]). Middle: Retina image with AMD (Source: National Eye Institute of the NIH [50]). Right: Retina image with diabetic retinopathy (Source: MESSIDOR [49])

What can the retina tell us? The most obvious answer is of course: changes and diseases happening in the retina itself. Retinal pathologies may affect one or more of the retina landmarks; macula, optic disc, vasculature, depending of the type of pathology. The most pressing eye problem affecting our society today are cataract, glaucoma, age-related macular degeneration (AMD) and diabetic retinopathy [34]. Figure 2.2 shows images of retina with AMD and diabetic retinopathy. AMD is a leading cause of blindness worldwide and is a common cause of blindness in people aged more than 50 years old [34]. A retina with this disease is recognized by the presence of drusen which appear as pale, yellowish lesions, found in both macula and peripheral retina [26]. Diabetic retinopathy is caused by complications of diabetes mellitus, which can eventually lead to blindness. It is the commonest complication of diabetes and is one of the leading causes of blindness [34]. Early signs of diabetic retinopathy are microaneurysms, small haemorharrges, cotton wool spots, exudates and new vessels [89].

2.3.2 Other Pathologies

The potential of retinal microvascular abnormalities as predictor or marker of other pathologies started as early as the 19th century when Marcus Gunn described the relations between retinal microvascular characteristics and hypertension, renal and cerebrovascular diseases [62, 63]. More recent researches have found more evidence in the associations between retina microvascular abnormalities with risk of hypertension, cardiovascular disease, cerebrovascular disease as well as mortality [47, 54, 56, 57, 59, 60, 61].

The ability of retina to act as a "window to the human body" is due to the fact that it shares similar anatomical and physiological characteristic with the cerebral and coronary circulations [47, 64, 65, 66, 67]. This advantage is explained by Keith, Wagener, and Barker[68] "because the arterioles are small and are difficult to visualize

in the peripheral organs—for example, in the skin, mucous membranes, and voluntary muscle— the retina, as seen through the ophthalmoscope, offers a unique opportunity for observing these small vessels clinically from time to time. Therefore, we think that certain visible changes of the retinal arterioles have been of exceptional value in affording a clearer clinical conception of altered arteriolar function throughout the body."

This has opened up whole new possibilities for the discovery of retina as an indicator of diseases elsewhere in the body.

2.4 Retinal Imaging

Numerous researches have proven direct ophthalmology to be unreliable and subjective especially in the detection of subtle retinal vascular changes [47, 69, 71]. Retinal photographs have been suggested to be more reliable in identifying lesions, and retinal vascular changes [47, 57]. Kagan et al [71] described large inter-observer (20–42%) as well as intra-observer (10–33%) variations in the assessment of different retinal lesions with direct ophthalmoscopy. In addition, digital retinal imaging allows patients' images to be stored which makes disease monitoring easier. Patients who stay in rural area where experts are not available can be diagnosed by having their retinal photographs taken and sent to experts in other countries for analysis.

Retina can be imaged with several methods:

- Fundus Photography

  Fundus images can be taken with either mydriatic or non-mydriatic camera. The size of field of the images is usually between 30° to 50° depending on the camera used. To capture a fundus image, the retina is illuminated and the reflected light is captured by a digital sensor. The digital sensor can be charge-coupled device (CCD) or complementary metal oxide semiconductor active pixel sensor (CMOS-APS) [58]. There are two types of retinal fundus images

(Figure 2.3), optic disc centered (field-1 type) and macula centered (field-2 type). All images used in this thesis are macula centered images.

Figure 2.3: Left: Field-1 type, optic disc centered retina image (Source: University of Michigan Kelogg Eye Centre [87]). Right: Field-2 type, macula centered retina image (MESSIDOR [49])

Color fundus images consist of three channels; red channel (R), green channel (G) and blue channel (B). When performing image processing on fundus images, we choose only green channel because it has good contrast whereas blue and red channel contain more noise in comparison [15, 90, 91]. Hence, throughout this thesis, only the green channel of the fundus images is used for all processing which includes vessel segmentation, fovea detection as well as artery-vein classification.

- Fluorescein Angiography

  Images are taken by injecting a dye into the patient's arm and the dye is then traced as it flows through the blood vessels in the retina. The dye used is fluorescein that absorbs blue spectrum of the light and emits yellow-green light. A series of retinal images are taken at an irregular interval of time as the dye travels though the blood vessels. It is especially useful to detect blood leakage in

the retinal vessels which can be viewed as leakage of the dye in the image. An example of fluorescein angiogram sequence is shown at Figure 2.4.

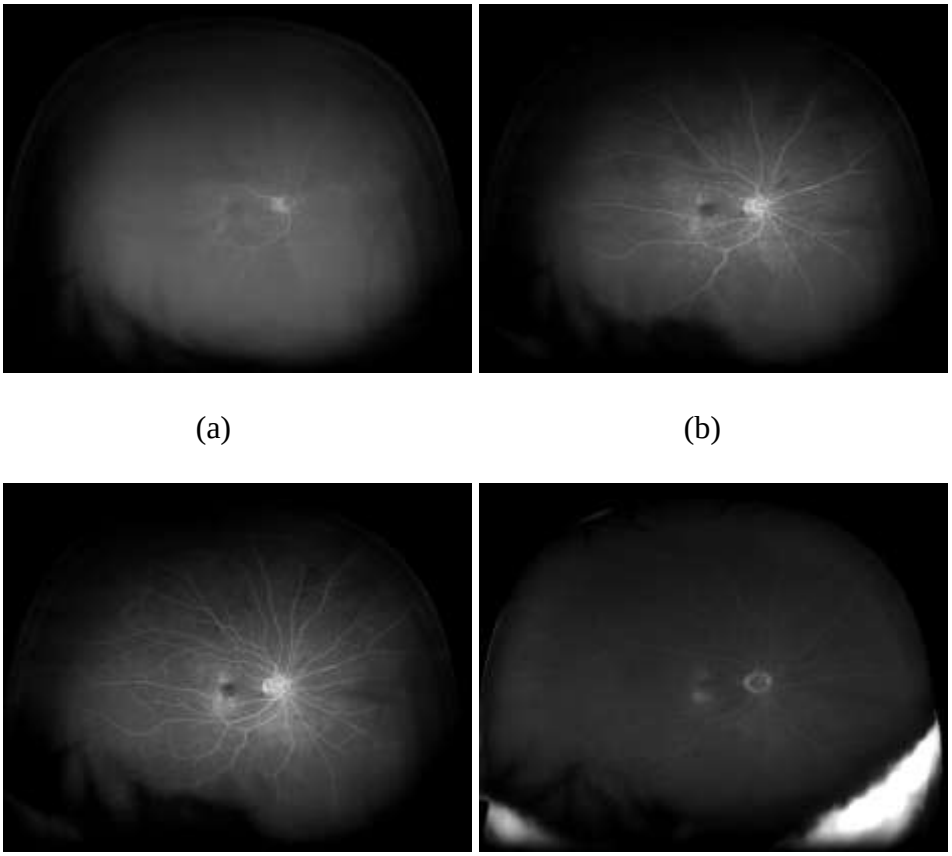

(a) (b)

(c) (d)

Figure 2.4: Four phases of fluorescin angiogram sequence: (a) arterial phase (b) arterio-venous phase (c) venous phase (d) late venous phase. (Source: Optos plc)

- Optical Coherence Tomography (OCT)

  This is a relatively new non-invasive method that captures 3D image of the retina. It produces cross-sectional images of the retina, which allows the thickness of different layers to be measured. This method has been used to test retina's response to various treatment methods. An example of optical coherence tomography is shown at Figure 2.5.

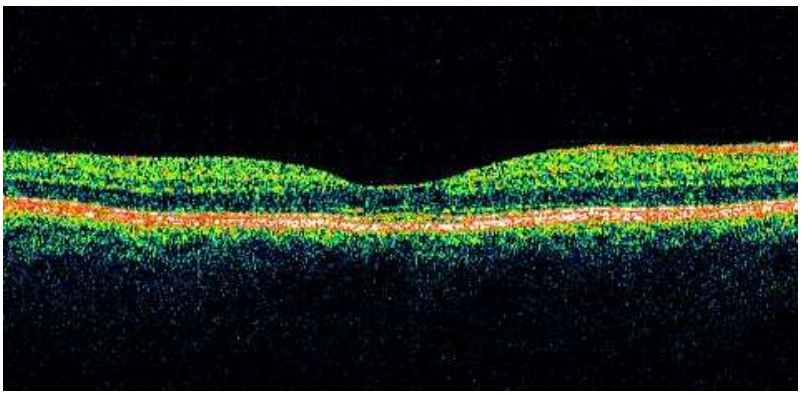

Figure 2.5: Optical coherence tomography of the fovea (Source: The Oeil project [92])

2.5 Automated retinal image analysis

Recent data has revealed that there are 37 million blind people and 124 million with low vision worldwide [34]. The main causes are cataract, glaucoma, corneal scarring, age-related macular degeneration, and diabetic retinopathy. This indicates the need for a more accurate, efficient and low cost retinal analysis systems capable to detect signs of pathologies especially in the early stage.

Automated retina image analysis is a promising solution because:

I. ***It is able to process large number of images at low cost operation***. One of the greatest expenditure in a screening program is the cost for trained manual graders [74], where they are often required to grade a large amount of images. Hence, computerized system can be used to help reduce the workload by eliminating images with no disease.

II. ***It is able to provide a more objective and standardized assessment*** of retinal images compared to diagnosis from direct ophthalmoscopy which tends to be subjective and unreliable [69, 70, 71, 72, 73]. Studies such as the Atherosclerosis Risk in Communities Study (ARIC Study) where retinal micro-vascular characteristics were evaluated from retinal photographs, using a standardized grading protocol, has proven that computer assisted quantification of generalized arteriolar narrowing showed high reliability in

the readings taken from the same subject at different times, as well as in intra-grader and inter-grader readings [93, 6].

III. ***It is able to provide advanced quantitative analysis of the retina***. Some quantitative analysis such as vessel tortuosity, fractal dimension of the vasculature and branching coefficients are hard to quantify with human eye or even manually on the retina photographs. Automated system with advanced image processing technique allows these to be done in a more systematic way.

Most of the work in automated retinal diagnosis has been emphasized on diabetic retinopathy [74]. Research in automated retinal analysis focuses mainly on automating the detection of lesions, or detecting features that relate to some diseases or progression of disease in the eyes. Early detection of these diseases will prevent possible blindness. To date, automatic image detection of retinal pathology has come a long way since its birth in the 1970s with more advanced and effective techniques being discovered ever since and is rapidly improving. However, progress in computer assisted system for retinal analysis is hard to justify because different studies reported accuracy in images of different qualities and different pathologies. Moreover, the accuracy reported by different authors often use different validation procedure, making comparison between algorithms difficult.

There remain challenges to be solved before automated retinal image analysis systems can be used for general clinical diagnosis. The challenges faced by researchers working in automated retinal image analysis are not only technical but also due to clinical limitations. In the clinical part, there exists ambiguity among ophthalmologist in the definition retinal feature, for example vessel tortuosity [95] and macula region [99]. Moreover, the same pathology may have different types of pigmentations on patients of

different ethnicity [34] and there is also variation in retinal features even in healthy images due to gender, and age [109, 110].

2.6 VAMPIRE: Vessel assessment and measurement platform for images of the retina

VAMPIRE is a tool that performs automatic quantification of retinal vessel properties with large collections of retina fundus camera images [1]. The project was started by the Computer Vision Group from the University of Dundee with the collaboration of four image processing groups and five clinical centres in the UK, Europe and Singapore. VAMPIRE has since been continuously developing with more retina image analysis modules being integrated and improved. VAMPIRE's interface designed for use by non-specialists on image processing (e.g, clinicians, geneticists). The system relies on the vasculature extraction developed by Soares et al [4] to automatically quantify different properties of the vascular network in the retina: vessel width, vessel tortuosity, branching angles, and branching coefficients.VAMPIRE has been used to run images of resolution ranging from approximately 400x400 to 3000x3000 pixels, acquired by various commercial instruments. These include fundus cameras (e.g., Canon CR-DGi nonmydriatic at 45_ FOV, TopCon TRC nonmydriatic fundus camera). This software had been used for various studies which includes diabetic retinopathy, AMD, and relation between retinal micro-vascular abnormalities with stroke, cerebrovascular disease and hypertension [51]-[60].

2.6.1 Optic Disc Location

The optic disc was detected using the algorithm developed in our group previously [16]. The optic disc is assumed to be a sub-region which is brighter than the local background, the contour is approximately elliptical, and vessels are present in its central part.

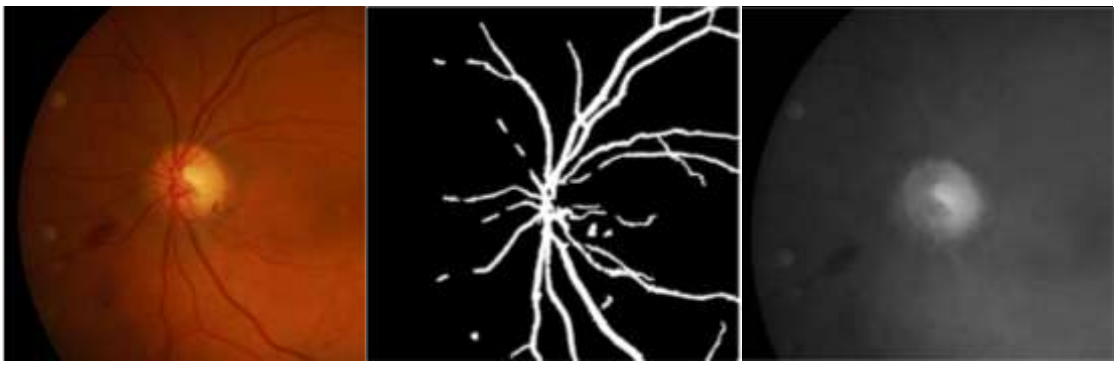

Figure 2.6: Left: the original RGB image. Middle: estimated vessel mask. Right: inpainted grayscale image (Source: [16])

Vessels are segmented by subtracting the top-hat filtered from the original component image and thresholding the result. The segmented vessels are then removed by inpainting (Figure 2.6). Final localization of optic disc is performed by optimizing the cost function which depends on internal/external contrast in the inpainted image and the gradient magnitude on the ellipse border.

2.6.2 Vasculature extraction

The vessel detection algorithm used in this software was developed by Soares et al [4]. To train the classification algorithm, 20 fundus images from the Lothian cohort [32] was manually segmented by Dr Tom MacGillivray and Dr Adria Perez Rovira.

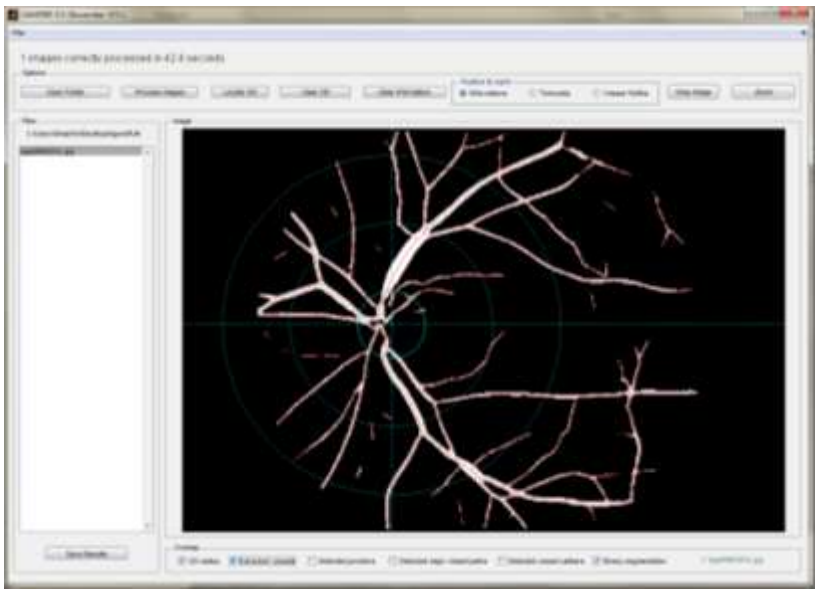

Figure 2.7: VAMPIRE interface showing the binary vessel map. Red lines are the vessel centerline. Blue circles indicate the retinal coordinate system centered on the optic disc

2.6.3 Vessel width

In order to obtain vessel width, a binary vessel map is first generated using VAMPIRE. Vessel width of a certain point in the centreline is estimated by the shortest length from the centreline to the vessel border as shown in Figure 2.8.

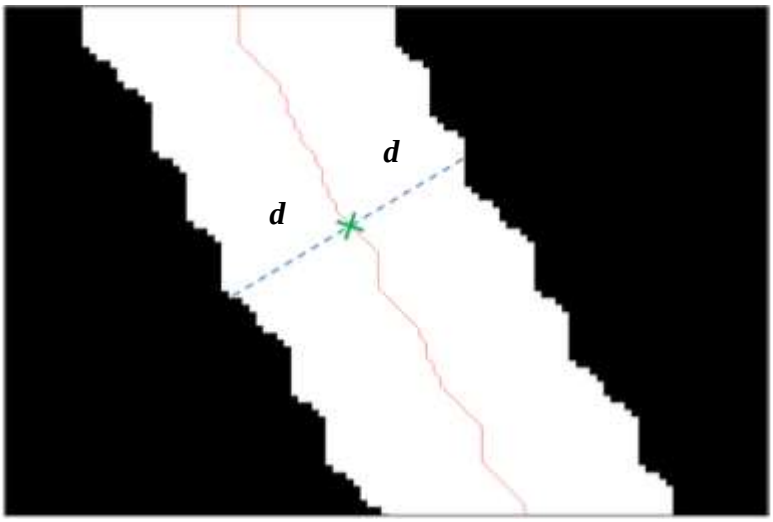

Figure 2.8: Vessel width estimation from binary vessel map (green cross shows the point of interest and dotted blue line shows the width of the vessel)

2.6.4 Branching angles and branching coefficients

Before calculating branching angles and branching coefficients, it is important to refine the location of branching point. To do this, VAMPIRE has implemented the approach presented by Tsai et al [101]. This approach generates a circular exclusion area around the bifurcations proportional to the width of the parent vessel (Figure 2.9). Vessel centerlines outside the circular exclusion area are used to estimate a straight line for each vessel branch. The new bifurcation location is estimated as the point that minimizes the distance to the three intersecting lines, as shown in Figure 2.9(b).

The largest vessel connected to the bifurcation is labeled as the parent vessel.

Branching angle is determined as the angle between centerline of the two child vessels, centered on the refined branching point. The bifurcation coefficient is determined as

$$b = \frac{w_1^2 + w_2^2}{W^2}$$

Where b =branching coefficient, w_1,w_2 = widths of child vessel, W = width of parent vessel. Width is calculated from the method presented in Section 2.6.3.

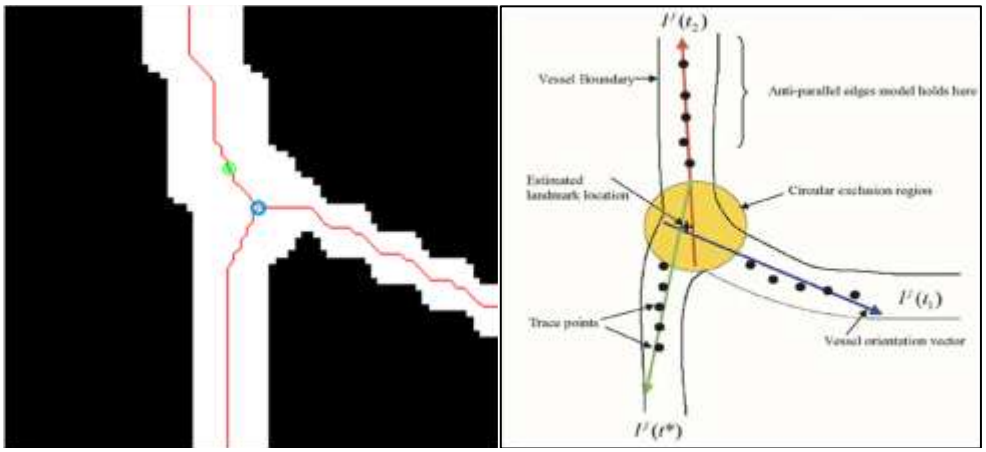

Figure 2.9: Left: Binary vessel segmentation showing the vessel centerline(in red), the detected branching point(in blue) and the refined location of the branching point (in green). Right: Diagram shows how the new location for the branching point is refined (Source: [101]).

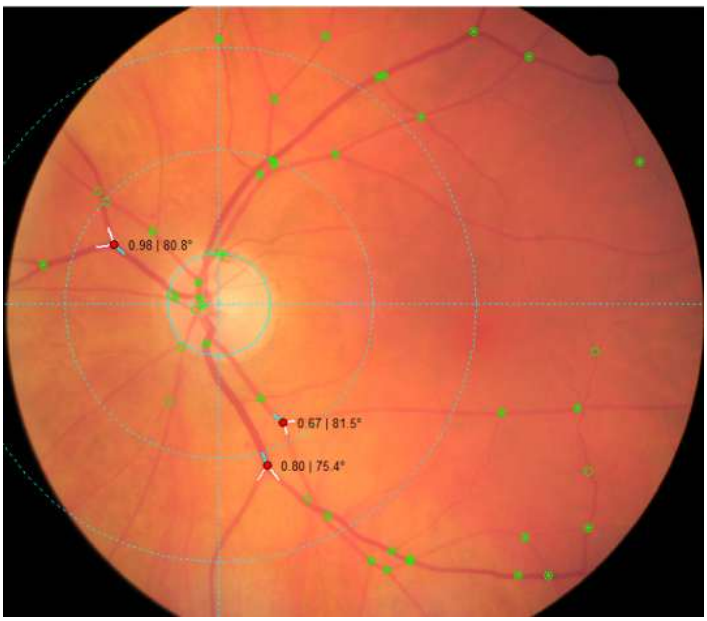

Figure 2.10: VAMPIRE interface showing a processed retina image (for branching)

In Figure 2.10, green circles are the detected junction points. Users are able to click on the junction points to obtain information of the junction, which are the branching

coefficient and branching angle. Selected junctions are shown as red circle, parent vessels are shown in green line and branches are shown in white line.

2.6.5 Vessel tortuosity

VAMPIRE implements novel tortuosity measure which combines both vessel skeleton curvature and vessel width, based on the work published by Trucco et al. [100]. The authors proposed that tortuosity depends not only on the vessel skeleton but also on the vessel width.

Figure 2.11: VAMPIRE interface showing a processed retina image (tortuosity)

In the Figure 2.11, yellow lines are the vessel centerlines whereas red lines are the selected vessel for tortuosity calculation. The tortuosity value is shown beside the selected vessel.

2.7 Conclusion

In this chapter, we have introduced clinical definition of the retina, background of retinal image analysis and highlighting its importance in aiding clinical diagnosis and research. We have also introduced and discussed the features of VAMPIRE, the automatic retina image analysis software previously developed in our group. This thesis focusses on developing more modules to be integrated into VAMPIRE.

CHAPTER 3

FOVEA DETECTION

3.1 About this chapter

In this chapter, we present a method to locate the center of the foveal region in retinal fundus images. The center of the foveal region is modeled as the center of the avascular region. Instead of using the appearance of the region, which is subject to image variations, we locate the fovea center based on an anatomical prior and vessel density. The latter is calculated with a Gaussian-weighted window, weighing vessel density more in the center of the window. The effect of varying standard deviation on the Gaussian weighting window is evaluated experimentally. Experiments with 116 images from a diabetes screening program show good accuracy (87% with distance error within 0.5DD). This chapter is organized as follows. Section 3.2 presents our motivation for macula detection as well as introducing clinical definition of macula and fovea. Section 3.3 discusses about the related work on fovea detection. Section 3.4 presents the methodology of our detection algorithm. Section 3.5 discusses the result of our algorithm and finally, the chapter is concluded in Section 3.6.

3.2 Introduction

The *macula* is a region temporal to optic disc and usually recognized as a dark spot in healthy retinal fundus images. Its center is known as the *fovea*. Ophthalmologists are interested in this region for several reasons. Firstly, it is the region responsible for central photopic and high resolution vision [26]; hence, any abnormal changes to this region may lead to serious vision loss or even blindness. Secondly, it is crucial to set up fundus coordinate systems, in which the horizontal axis goes through the optic disc and

the fovea. Such coordinate systems are important to characterize the spatial distribution of lesions, such as the grading of diabetic retinopathy. Thirdly, automatic detection of fovea would contribute to the efficient, semi-automatic analysis of large numbers of retinal images.

Although there is no ultimate agreement on the definition of the macular-fovea region, there is still a general anatomical structure on which we can base our detection algorithm. The macula is a region that covers four main anatomical regions: *fovea centralis, fovea, parafovea*, and *perifovea*. At the center of the macula is the fovea which is regarded as having the same size as the optic disk [29] and which contains an avascular area. Hence, we formulate the fovea localization problem as one of locating the center of an avascular zone [26] with the size of the optic disc within a pre-defined search region. The avascular zone is defined as the zone with least vessel density (Figure 3.1).

Figure 3.1: Left: retinal image showing the anatomical region of the macula (fovea, parafovea, and perifovea). Right: associated vessel map computed automatically. (Source: TENOVUS)

3.3 Related work

The current macula-fovea detection algorithms in the literature can be grouped into three main approaches: detection using macula appearance [25, 23, 18], detection using vessel structure [24], and detection using a combination of both [19, 20, 21]. Algorithms using macula-fovea appearance model the center of the fovea as the region with the

darkest pixel intensity. However this assumption does not work in general; e.g., some macular diseases make the macular region appear lighter than usual or severely pigmented (Figure 3.2).

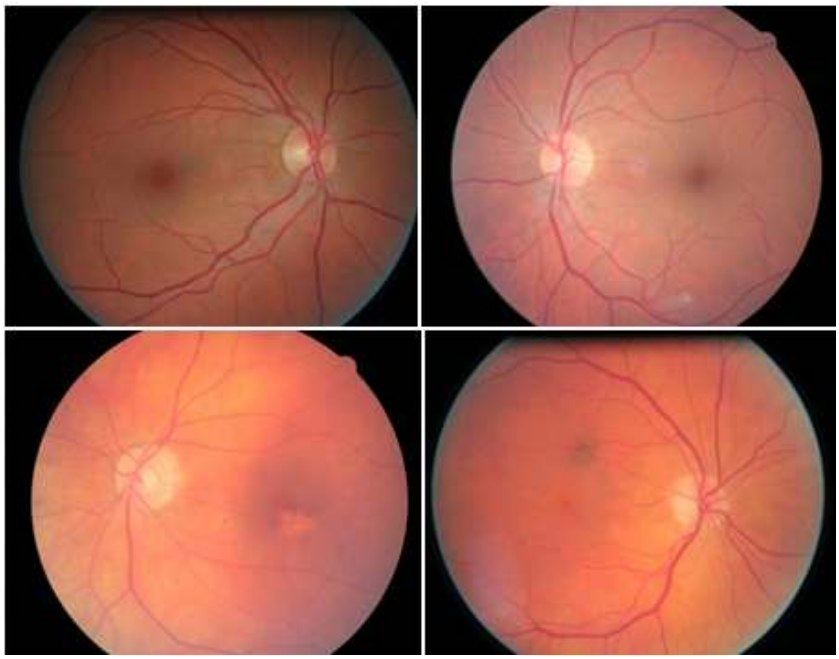

Figure 3.2: First row: Healthy retina images which show macula-fovea region as clear dark spot. Second row: Diseased retina images where the appearance of macula-fovea region is no longer obvious but can still be recognized by its position relative to optic disc and main vessel (Source: TENOVUS)

Algorithms that use the vessel network to find the fovea center fit a low-order curve (e.g., parabola, ellipse) to the main vessel arcades, then, locate the fovea center as a point that lies at a given distance along the parabola main axis. For instance, Sinthanayothin *et al* [18] fix the disc-to-macula distance to disc-diameter ratio (DM:DD) as 2.5 disc diameters (DD); Li *et al* [19] fix a ratio 2DD, whereas Ying *et al* [21] takes the range between 2DD and 2.5DD. However, the DM:DD ratio varies quite significantly between individuals due to different age and pathology in the eye. Patients with physiological macrodiscs usually have a smaller DM:DD ratio and have been reported to have a lowest value of 1.84DD in [28]. For patients with optic nerve

hypoplasia, for example, a condition where the optic nerve is underdeveloped and the OD appear abnormally small, the DM:DD ratio has been reported to be more than 3DD and to have a largest value of 4.2DD in adults [30].

Algorithms that combine information from vessel network and macula-fovea appearance generally find the main vessel arcade and then detect fovea center as a region of darkest pixel intensity within the main vessel arcade [19, 20], or as a dark region with low vessel density within the main vessel arcade [21].

3.4 Methodology

3.4.1 Algorithm overview

First, the optic disc contour is approximated by an ellipse and located using our algorithm reported elsewhere [16]. A vasculature map is calculated using vessel segmentation algorithm developed by Soares et al [15] to obtain the location of blood vessels. Both optic disc detection and vessel segmentation is performed within VAMPIRE. A parabola with vertex in the centre of the optic disc is then fitted to the vessel map to locate the approximate path of the main arcade visible. A search region for the fovea is then formed from anatomical priors and posterior probabilities estimated from sample images. Within the search region, a cost is calculated for each candidate position; the lowest-cost one is taken as the best estimate of fovea position. Details of each stage are given in the following sections. The overall fovea detection algorithm is shown in Figure 3.3. Henceforth, *r* will denote the radius of the optic disc, DD denotes disc diameter and DM:DD denotes disc-to-macula distance to disc-diameter ratio.

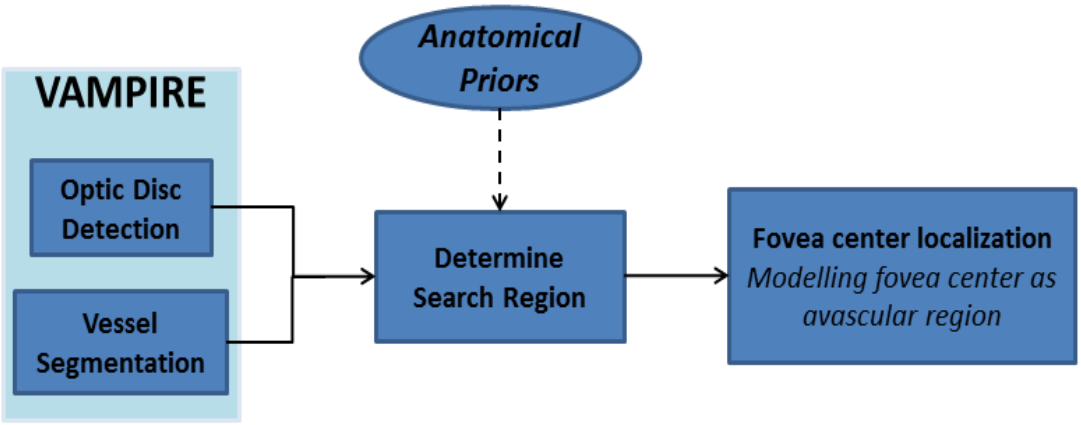

Figure 3.3: Overall fovea detection algorithm

3.4.2 Determining a search region

We consider three anatomical constraints to identify a search region for the fovea. First, we establish a range for the disc-to macula distance to disc-diameter distance ratio (DD:DM). Second, we constrain the search region to be within the parabola approximating the main arcade (Figure 3.5). Third, following [27], we further confine the search region to be located below the upper boundary of optic disc. We obtain the final search region by intersecting the three constraints. Within it, candidate pixels are sampled for cost evaluation with a spatial step of 1/6 of the optic disc radius (Figure 3.6).

3.4.2.1 Disc to Macula ratio (DM:DD)

We estimated the probability distribution for DM:DD from a sample set of 126 screening images, which are not used for testing the fovea location algorithm. The images chosen have good quality and the fovea is obvious, to ensure that the DM:DD information we obtain is as accurate as possible.

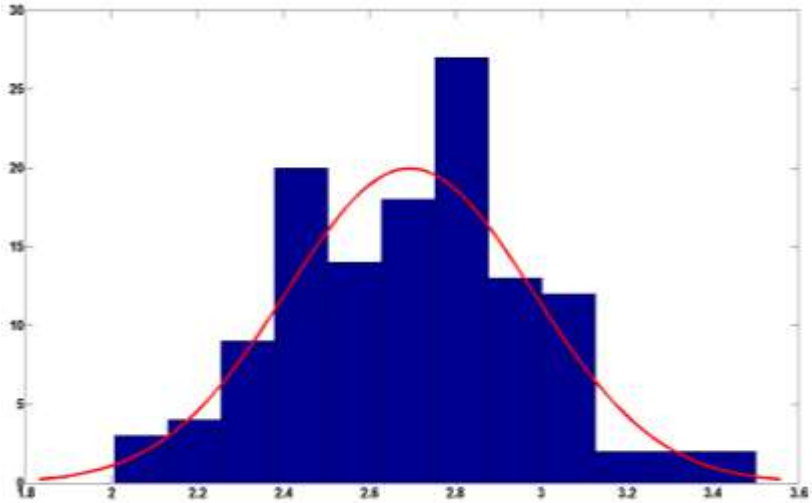

(a)

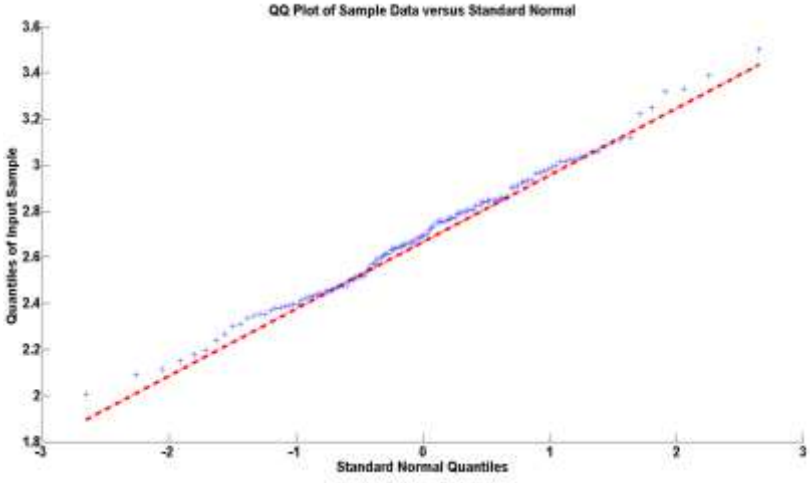

(b)

Figure 3.4: (a) Distribution of DM:DD ratio obtained from 126 sample images. (b) QQ plot of the DM:DD ratio obtained from the sample images. Red line is the theoretical quantile from normal distribution and blue dots represent the sample quantile.

We approximate this distribution with a Gaussian (Lilliefors test at 5% significance level, p value= 0.430). Liliefors is used to test the null hypothesis that the distribution of the data comes from a normally distributed population. Figure 3.4(a) shows the graphical illustration of the sample distribution which approximates a normal

distribution. Figure 3.4(b) shows the QQ plot of the sample data. It can be seen that the data (dotted blue) is close to the red linear line which represents the normal distribution.

Assuming the data to be normally distributed from the statistical tests, we then fix the DM:DD range within 3 standard deviations from the mean, i.e., 1.82DD to 3.56DD.

3.4.2.2 Main Arcade Approximation

The main arcades are the large retinal vessels emerging from the optic disc and lying within areas of with high vessel density [21] and can be approximated with a parabola. To select the points to use for parabola fitting, the vessel binary map is first skeletonized. A $r \times r$ square neighbourhood is considered around each skeleton point, and vessel density and average width estimated within it. A vessel density map and an average width map are then calculated and combined by linear summation. Vessel points are then clustered into four clusters using the combined map and a K-means algorithm. Points in the highest-valued cluster are chosen for parabola fitting using the following equation:

$$a[(x-h)\sin\theta + (y-k)\cos\theta]^2 - [\cos\theta(x-h) - \sin\theta(y-k)] = 0. \quad (1)$$

Here, θ is the orientation angle of the parabola axis with respect to the *x* axis of the image, and *a/4* is the focal length. The parabola vertex has co-ordinates *(h,k)* and is chosen as the point inside the optic disc with the highest vessel density. This is estimated by the number of vessel pixels in the vessel map within a $r \times (r/2)$ search window. The fit estimates the two parameters, a and θ. The parabola is fitted by minimizing the algebraic distance, i.e., the residual of Equation (1) when numerical values are used, with the Nelder-Mead algorithm [31].

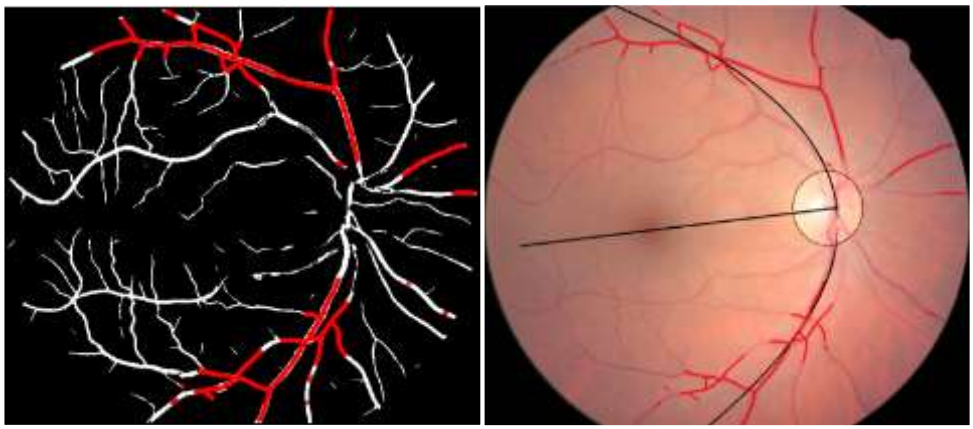

Figure 3.5: Left: Retinal vessel map with vessel pixels chosen for arcade location (parabolic fit) in red. Right: Result of parabolic fit (parabola and its axis shown in black).

3.4.2.3 Final Search Region

In order to establish the final search region, we combined the anatomical priors previously discussed: fovea lies within a certain range of DM:DD from optic disc and within the main arcade. We also incorporated another anatomical prior to further confine the search region to be below the upper boundary of the optic disc [27]. Within the search region, candidate pixels are sampled for cost evaluation with a spatial step of 1/6 of the optic disc radius. The method for cost calculation is explained in Section 3.4.4.

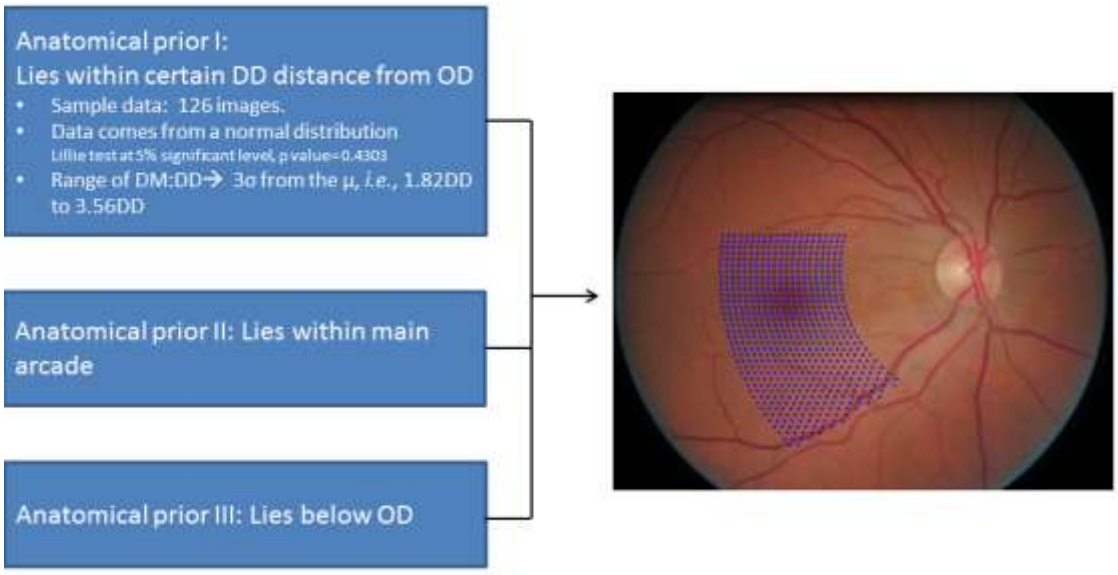

Figure 3.6: Combination of three anatomical priors to obtain the final search region

3.4.4 Fovea center localization

To locate the fovea, we evaluate each sampled location in the search region (Figure 3.6). As the fovea is taken to be about the size of the optic disc (Section 3.2), a square window of optic disc size is centered on each point of the search region and evaluated. As blood vessels are less visible in the fovea than in surrounding regions, we compute the vessel density from the binary vessel map and apply with Gaussian weights, so that higher weights are given to central points where the avascular region is expected (Figure 3.7). The weights are normalized so that they sum to one.

Figure 3.7: Illustration of vessel density weighting. Left: Gaussian mask profile (red is largest). Centre: binary vessel window. Right: weight of each vessel point (red is largest).

The final vessel density estimate for a candidate location is the sum, over the square window, of the point wise product of the weights and the binary vessel map. The location with the lowest vessel density within the whole search region is taken as the best estimate of the center of the fovea. Figure 3.8 gives an illustration of the search algorithm.

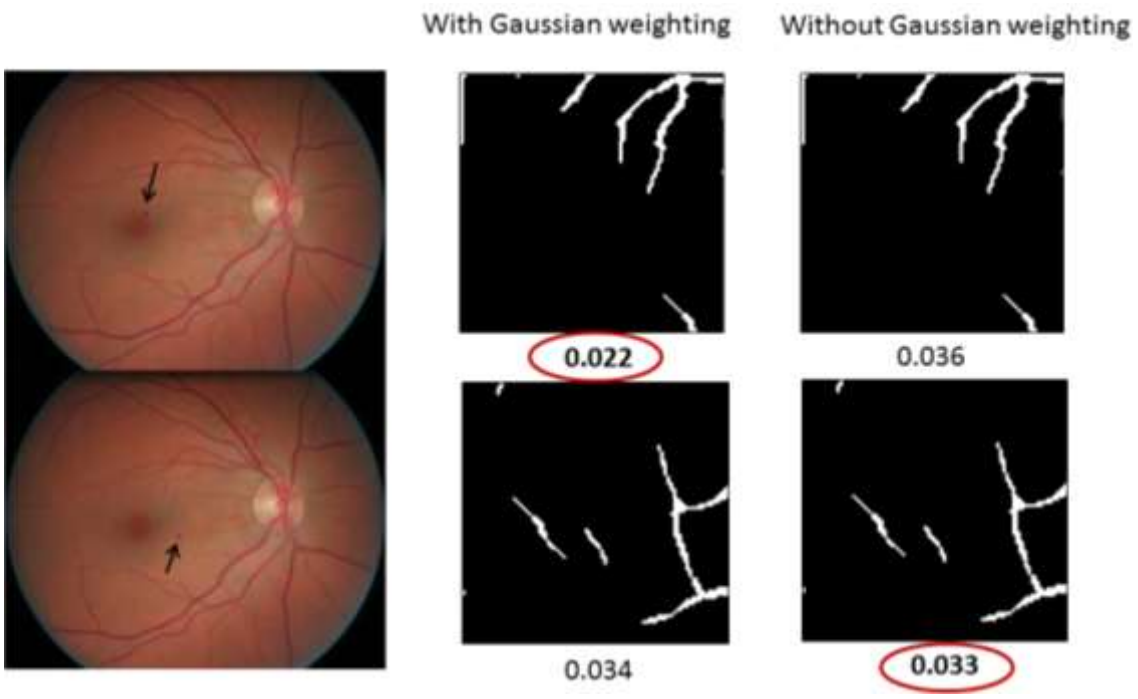

Figure 3.8: Illustration of the search algorithm.

In Figure 3.8, the first row represents a search position closer to the fovea center whereas the second row represents a search position further from the fovea center. Column 2 and 3 show calculated vessel density from the patch, one with Gaussian weighting and another without. The algorithm is designed to choose the position with a smaller magnitude of vessel density. Hence, if vessel density calculation is not Gaussian weighted, it will choose any random position with low vessel density instead of a position with an avascular region in the center. This will result in the algorithm choosing the wrong position. An example is shown in Figure 3.8 where algorithm chose the position in the second row, which is further away from the fovea compared to the position in the first row.

3.5 Experimental result

3.5.1 Materials

We evaluated our algorithm on 116 color fundus images from the TENOVUS dataset. The images we used were of high resolution (2336x3504) and were of type-2 field, i.e., centered on the macula. To test the algorithm performance with varying quality, the test images were divided into three difficulty (quality) levels: good (66 images), medium (30), and difficult (20). Quality was determined by the visibility and integrity of the macula region.

3.5.2 Ground truth

A software tool was developed to obtain ground truth input from annotators.

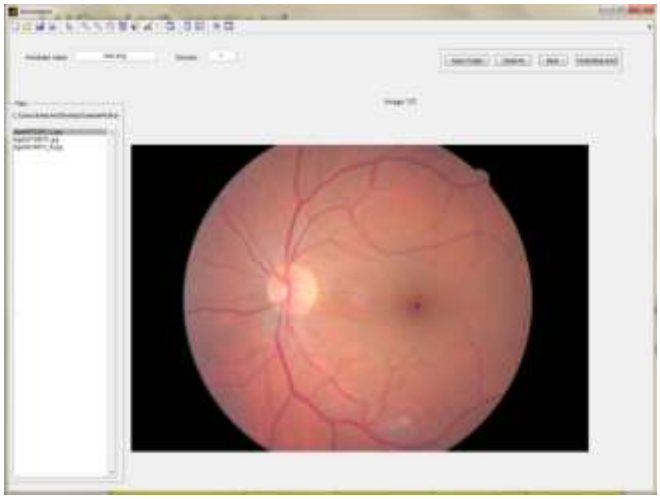

Figure 3.9: Interface tool to obtain ground truth for fovea position

Above is a screenshot of the tool where observers were asked to mark the fovea centre (shown as blue point in image. We compared the results from our algorithm with annotations provided by 2 observers, a practicing ophthalmologist and a trained image processing expert. To estimate intra-observer variability the images were annotated twice by each observer in independent sessions. The two observers acted independently.

Intra-observer	Good	Medium	Difficult	All Images
Observer 1	4.42% ± 2.98%	8.09% ± 10.05%	10.63% ± 8.01%	6.44% ± 6.85%
Observer 2	5.99% ± 3.85%	6.96% ± 5.03%	10.37% ± 7.72%	6.99% ± 5.21%
Inter-observer	**Good**	**Medium**	**Difficult**	**All Images**
Observer 1 vs Observer 2	5.52% ± 3.09%	8.66% ± 4.48%	16% ± 6.36%	8.14% ± 6.36%

Table 3.1: Euclidean distance error between intra observer and intra observer, as percentages of disc diameter.

Table 3.1 shows the paired Euclidean differences for intra-observer and inter-observer. The difference is expressed as mean±SD in % of the disc diameter. The mean difference increases from good to difficult images for both intra- and inter-observer figures, reflecting the increasing uncertainty of location of the fovea center as the image quality degrades.

We used the Bland-Altman method to measure the agreement between intra-observer and inter-observer. The analysis was performed separately for X and Y values of the fovea center coordinate.

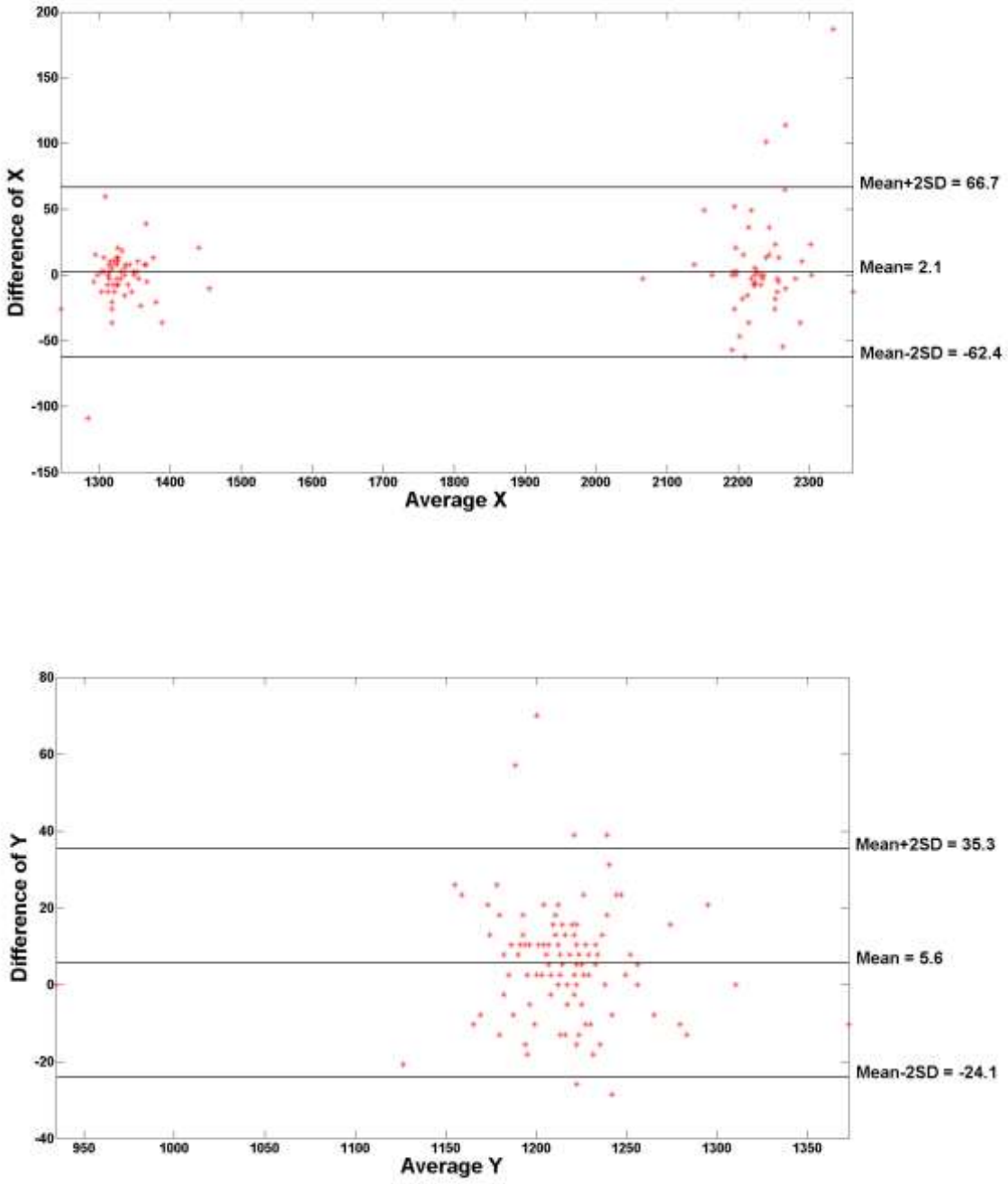

Figure 3.10: Bland Altman plots of X and Y values for intra-observer difference in Observer 1.

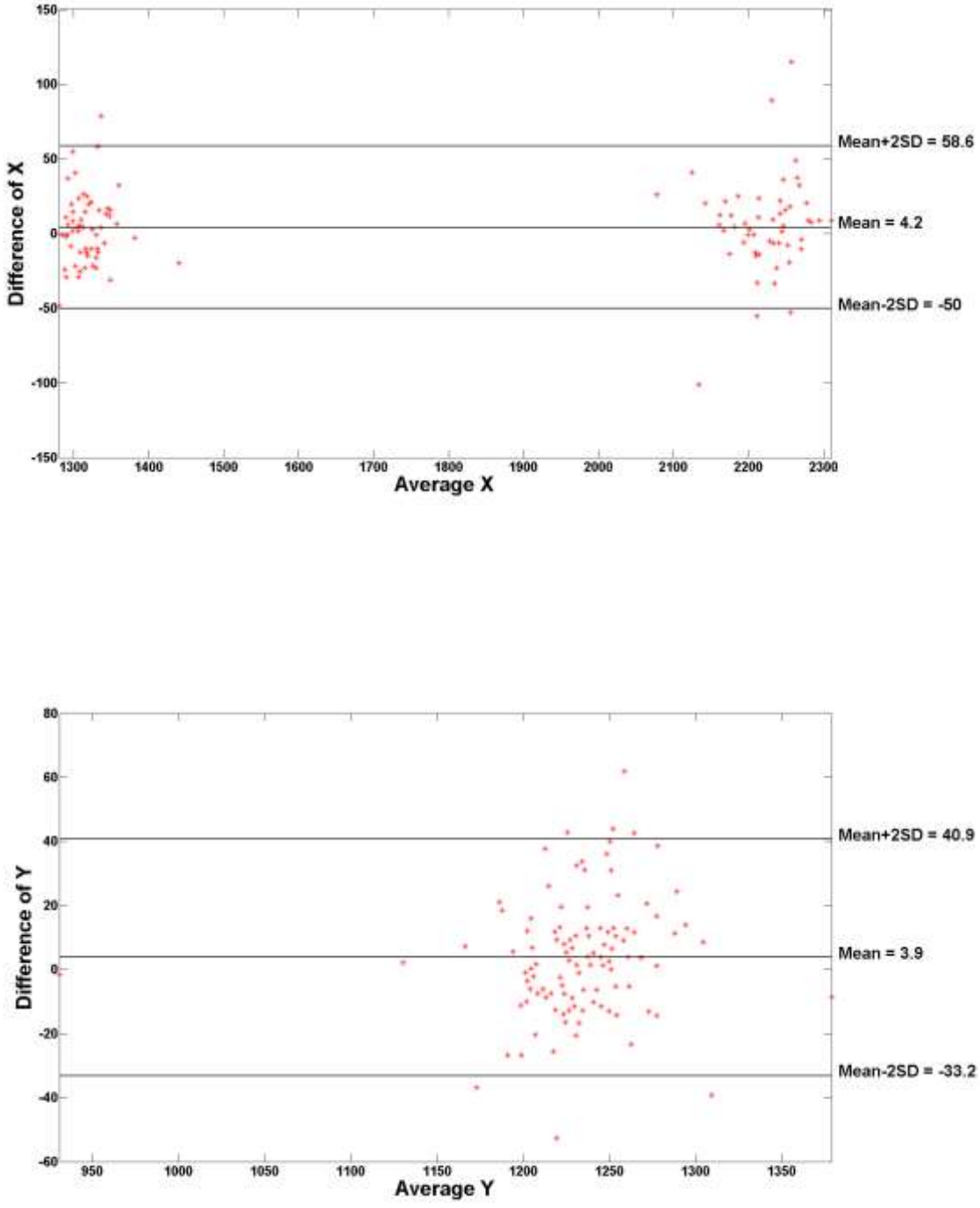

Figure 3.11: Bland Altman plots of X and Y values for intra-observer difference in Observer 2.

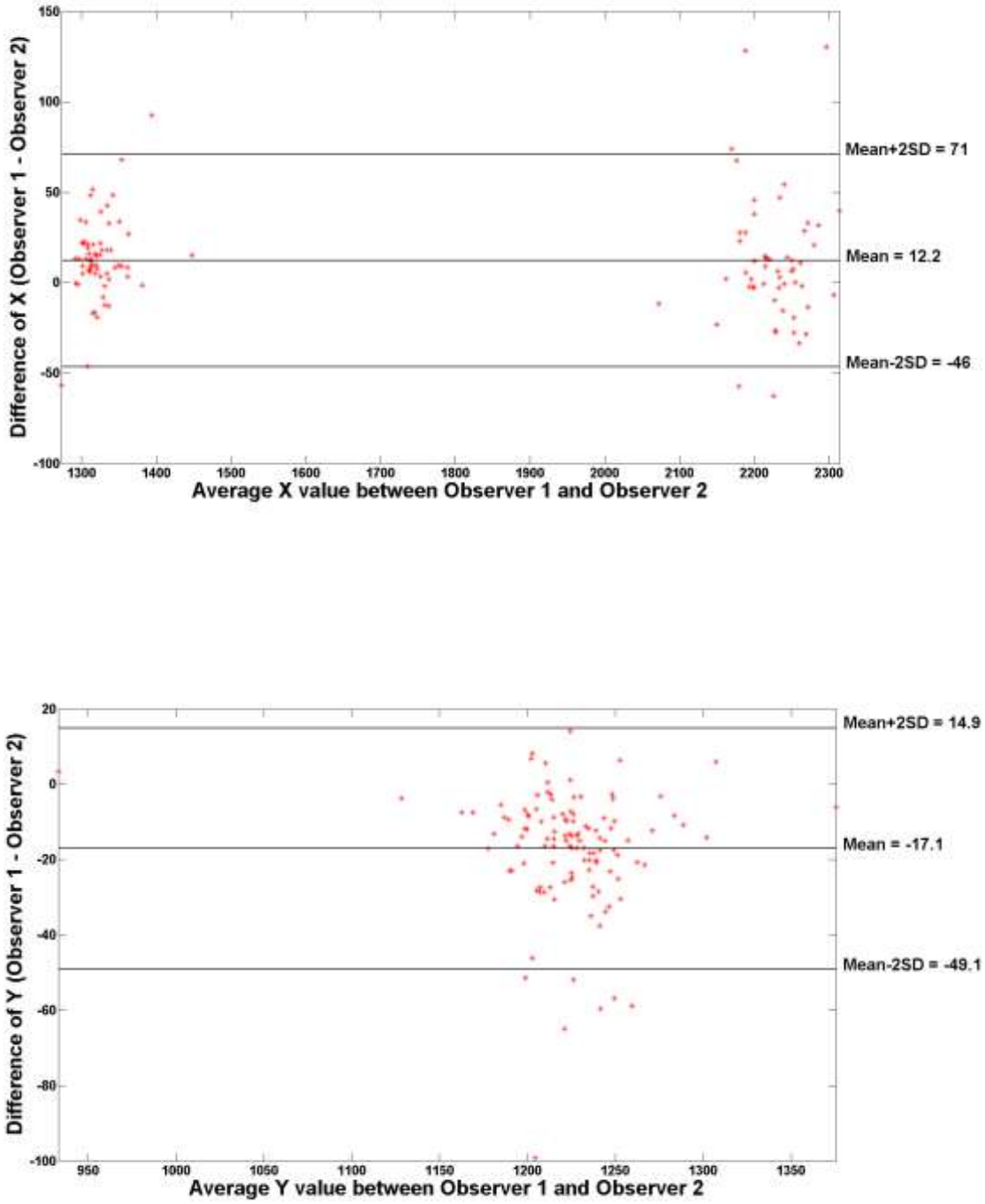

Figure 3.12: Bland Altman plot of X and Y value for inter-observer difference

Figure 3.10, 3.11 and 3.12 show Bland-Altman plots, respectively, for intra- and inter-observer differences for X and Y values, where X and Y are the co-ordinates of the points selected as fovea center. The two clusters for the X plots reflect the different location of the fovea in left and right eyes. The inter-observer differences have a larger mean than intra-observer differences, as expected, but the limits of agreement (mean±2SD in unit of pixel) are comparable. For example, the limit of agreement of X value for Observer 1 is between -62.4 and 66.7 pixels. In disc diameter units, the limit of agreement is expressed as -0.16DD and 0.17DD, which is small enough for us to be confident that there is strong agreement between the two annotations taken by Observer 1. The limits of agreement are also comparatively small for Observer 2 (-0.13DD to 0.15DD) as well as for inter-observer difference between the two observers (-0.12DD to 0.18DD).

3.5.3 Determining the optimal weighting Gaussian

To determine the optimal size of the weighting Gaussian window, we plotted the difference program-observer against different sizes of the Gaussian weighting window, given by its standard deviation, σ. This provides an appreciation of the algorithm performance at varying spatial scales. Smaller standard deviations put higher emphasis on smaller, more localized central regions.

	Observer 1_1				Observer 1_2				Observer 2_1				Observer 2_2			
σ	**Good**	**Med**	**Diff**	**Average**	**Good**	**Med**	**Diff**	**Average**	**Good**	**Med**	**Diff**	**Average**	**Good**	**Med**	**Diff**	**Average**
R/8	0.742	0.633	0.450	0.664	0.773	0.633	0.450	0.681	0.758	0.633	0.450	0.673	0.712	0.733	0.450	0.672
R/4	0.758	0.667	0.400	0.673	0.788	0.667	0.450	0.698	0.773	0.700	0.500	0.707	0.758	0.733	0.550	0.716
R/2	0.758	0.700	0.600	***0.715***	0.742	0.667	0.650	***0.707***	0.773	0.633	0.650	***0.716***	0.742	0.767	0.650	***0.733***
R	0.758	0.533	0.550	0.664	0.742	0.533	0.550	0.656	0.773	0.533	0.600	0.681	0.682	0.600	0.650	0.655
2R	0.682	0.567	0.550	0.629	0.652	0.567	0.550	0.612	0.697	0.500	0.600	0.629	0.636	0.600	0.650	0.629
Without Gaussian	0.667	0.600	0.550	0.629	0.621	0.533	0.500	0.578	0.697	0.500	0.500	0.612	0.621	0.600	0.550	0.603

Table 3.2: Fraction of images with distance error within 25% of the optic disc diameter, for varying σ value. "Observer 1_2" for example, means "second-time annotations from Observer 1"

	Observer 1_1				Observer 1_2				Observer 2_1				Observer 2_2			
σ	**Good**	**Med**	**Diff**	**Average**	**Good**	**Med**	**Diff**	**Average**	**Good**	**Med**	**Diff**	**Average**	**Good**	**Med**	**Diff**	**Average**
R/8	0.894	0.833	0.750	***0.853***	0.909	0.867	0.700	0.862	0.924	0.833	0.700	***0.862***	0.924	0.833	0.650	***0.853***
R/4	0.909	0.800	0.700	0.845	0.924	0.800	0.700	0.853	0.924	0.800	0.650	0.845	0.924	0.800	0.650	0.845
R/2	0.909	0.800	0.750	***0.853***	0.924	0.833	0.750	***0.870***	0.924	0.800	0.700	0.853	0.924	0.800	0.700	***0.853***
R	0.894	0.767	0.650	0.819	0.909	0.767	0.650	0.828	0.909	0.767	0.700	0.836	0.909	0.767	0.700	0.836
2R	0.894	0.767	0.650	0.819	0.909	0.767	0.650	0.828	0.879	0.767	0.700	0.819	0.909	0.767	0.700	0.836
Without Gaussian	0.894	0.800	0.650	0.828	0.894	0.800	0.650	0.828	0.864	0.800	0.700	0.819	0.894	0.800	0.700	0.836

Table 3.3: Fraction of images with distance error within 50% of the optic disc diameter, for varying σ value. "Observer1_2", for example, means "second-time annotation from Observer 1"

Table 3.2 shows the fraction of images for which the distance error between the program estimate and the observer annotation is within 25% of the optic disc diameter (approximately 382 pixels in the test images) from the center, computed for 5 different σ values of the Gaussian weighting window as well as without the Gaussian weighting, for the 3 image quality classes. Table 3.3 shows the fraction of images for which the distance error is within 50% of the optic disc diameter from the center. In Table 3.2, the Gaussian window with σ = r/2 has the best average performance; in Table 3.3, the Gaussian windows with σ = r/2 and σ = r/8 achieve equal scores. Hence, we chose the Gaussian window with σ = r/2 as the best performing algorithm because it performs best even in a stricter condition (25% DD).

3.5.4 Result and discussion

The detection accuracy was quantified by the distance between the fovea center detected by the algorithm and the ground-truth fovea center. Figure 3.13 and figure 3.14 shows the distance (difference) histograms and associated cumulative histograms for σ = r/2. The x-axis of the histograms is in disc diameter (DD) unit. The cumulative histograms shows that 90% of the error histogram lies within 0.35DD (for both observers) for good quality images, 0.73DD (observer1) and 0.8DD (observer2) for medium quality, 0.8DD (observer1) and 0.73DD (observer2) for difficult quality. Although for observer 2 the cumulative error for medium quality images is higher than that of difficult quality images, the medium quality images has higher fraction of images at lower distance error (Figure 3.14).

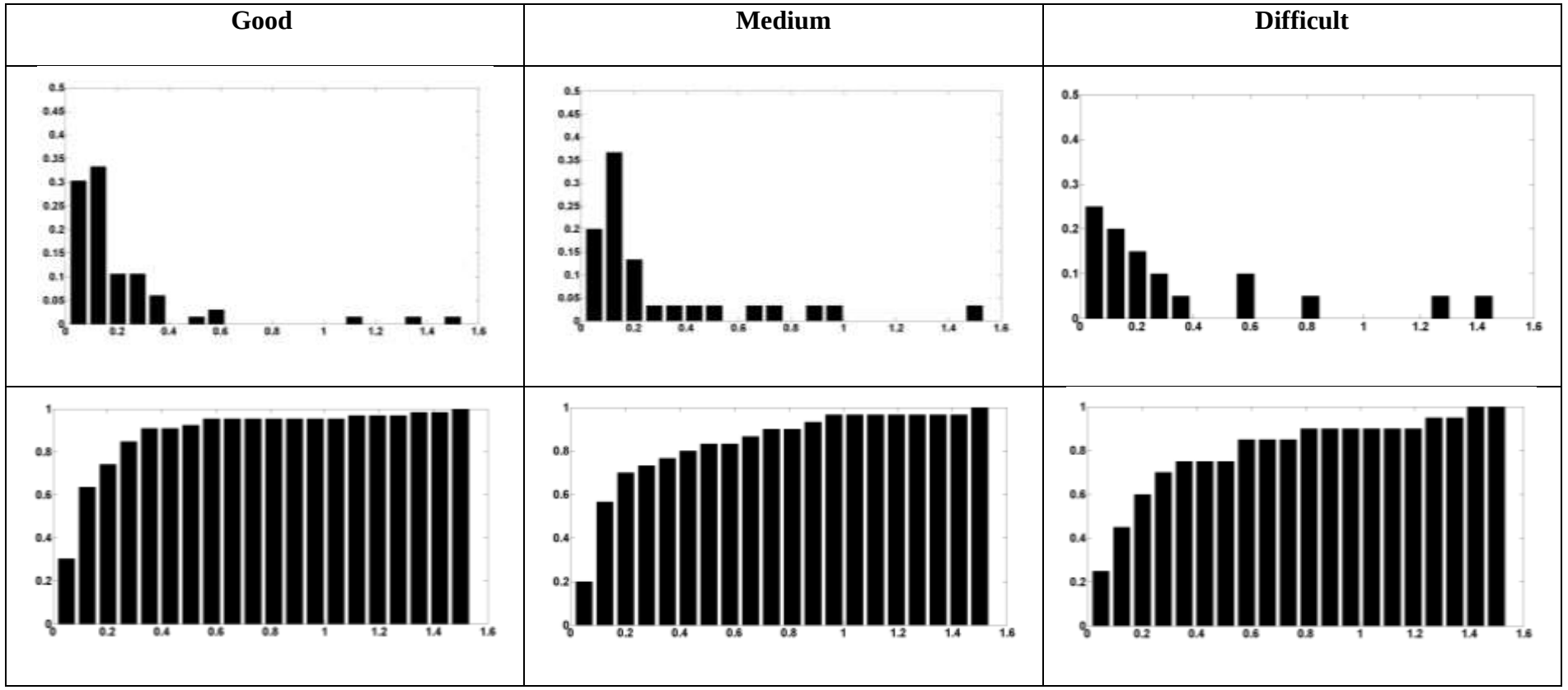

Figure 3.13: Result for Observer 1. First row: Histograms of distance error per quality class for σ = r/2. Second row: corresponding cumulative histograms. X axis values are in OD diameters (1 OD diameter ≈ 382 pixels).

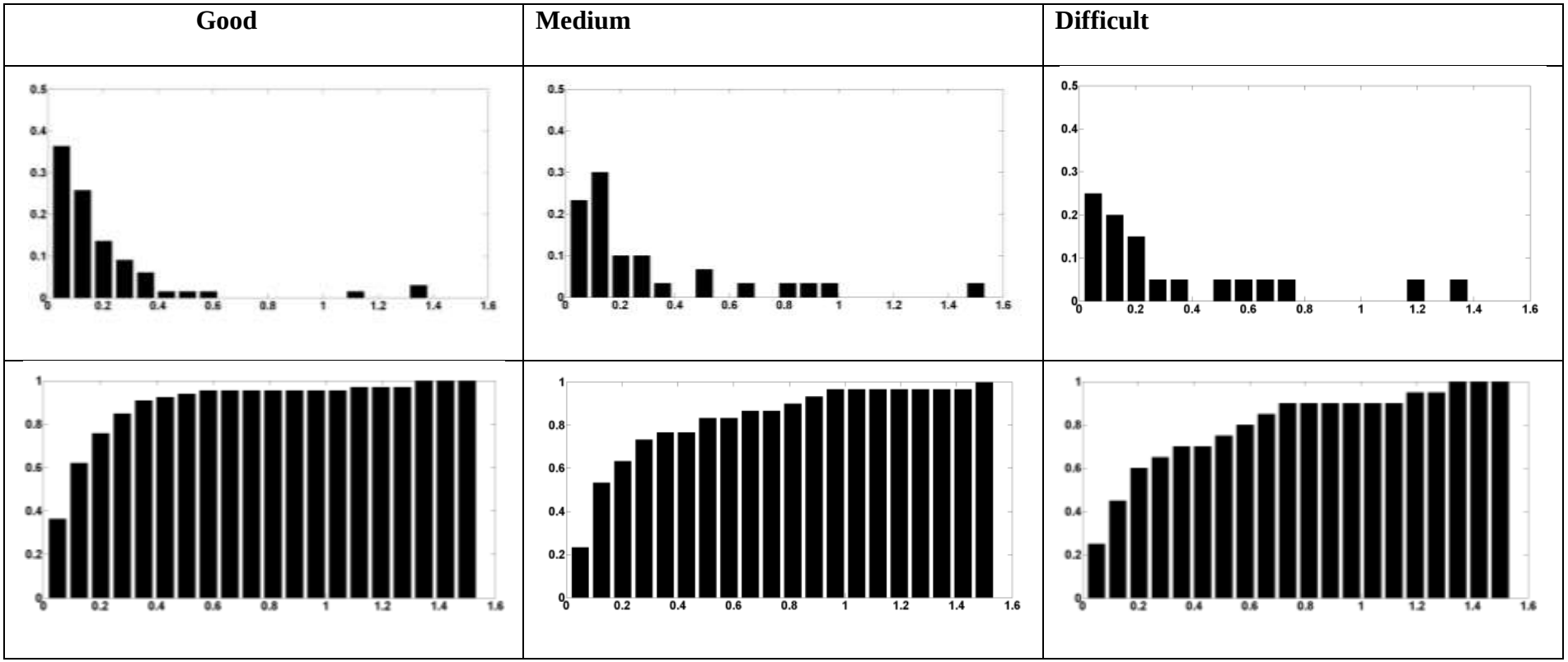

Figure 3.14: Result for Observer 2. First row: Histograms of distance error per quality class for σ = r/2. Second row: corresponding cumulative histograms. X axis values are in OD diameters (1 OD diameter ≈ 382 pixels).

Finally, Figure 3.15 illustrates the results of the automatic fovea detector on 3 images from each of the 3 quality classes.

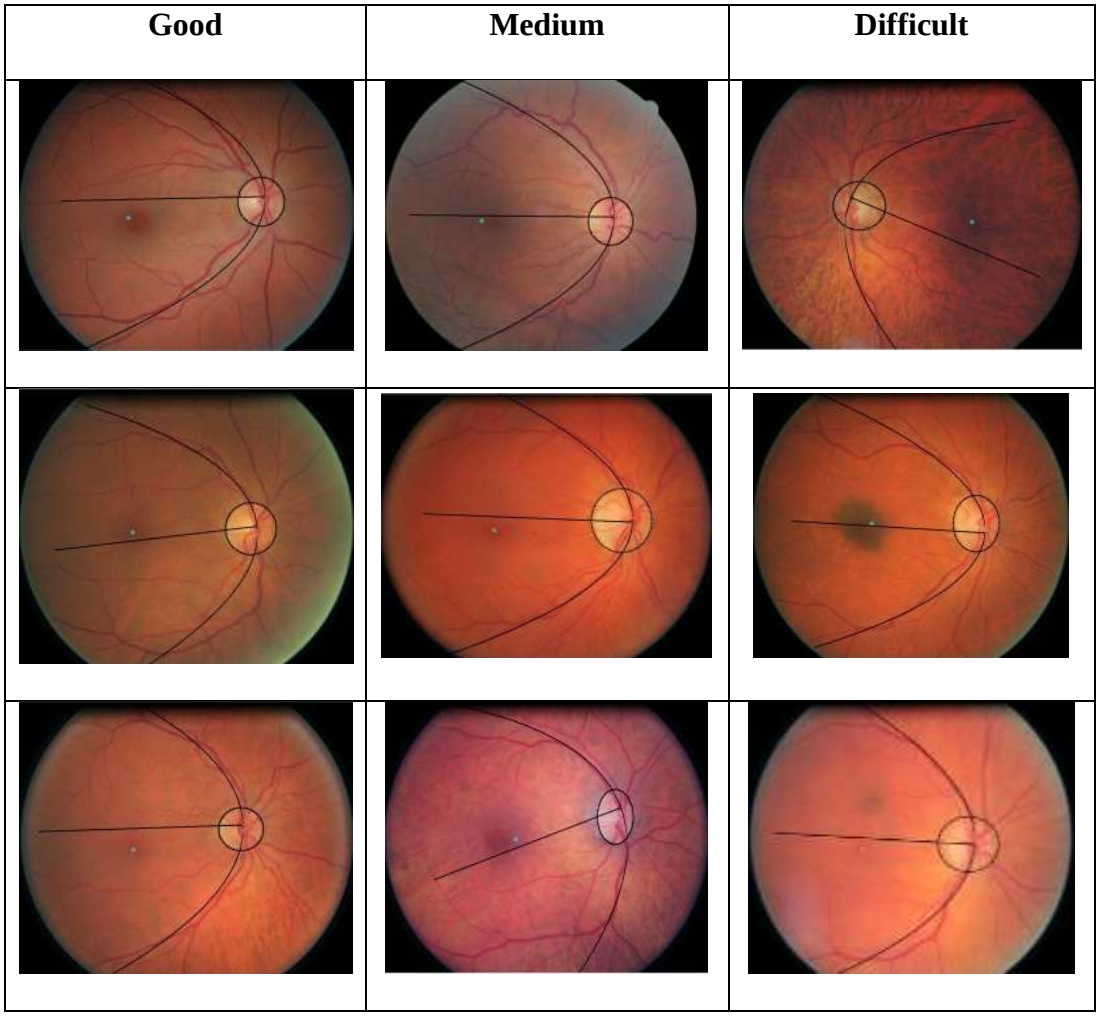

Figure 3.15: Result of fovea detection algorithm on 3 different quality images. Shown in each image is the OD boundary, fitted parabola and parabola axis (in black) and detected fovea center, shown as the blue point.

3.6 Conclusion

In this chapter, we presented a fovea detection algorithm utilizing prior anatomical information of the fovea. Experimental results are evaluated on ground truth from 2 annotators. We found from experiment that modeling the fovea region with Gaussian template of size r/2 produces the best result. From the experimental results, we conclude that the proposed algorithm is a potentially effective method to locate the fovea center in retinal images of various qualities. Results are dependent on the quality of the vessel segmentation used; therefore, for retina images in which the vasculature is not clear, the algorithm may not be able to detect the correct foveal avascular region accurately. Moreover, the appearance of the avascular region may be severely altered in retinas of patients with advanced-stage macular diseases [27]; in some cases, however, our algorithm was still capable to generate reasonable location estimates (e.g., Fig. 3.15, middle row, right). In the following chapters, we will present our work on computer-assisted arterio-venous ratio (AVR) estimation and artery-vein classification.

CHAPTER 4

TOOL FOR ARTERIO-VENOUS RATIO (AVR) ESTIMATION

4.1 About this chapter

This chapter describes the method and steps involved to obtain arterio-venous ratio (AVR). We developed a user interface tool to allow user to select vessels and branching points for AVR estimation. These vessels and branching points are then processed by VAMPIRE to obtain the corresponding vessel widths and branching coefficients. The AVR is then estimated using the protocol devised by Knudtson *et al* [2]. This tool was developed to aid in the clinical research of the relation of AVR with pathologies (i.e, hypertension and cerebral atrophy). This chapter is organized as follows. Section 4.2 introduces arterio-venous ratio (AVR) and its significance in clinical research. Section 4.3 discusses about the AVR estimation protocol from the literature and explains our choice of method for AVR estimation used in our system. Section 4.4 presents our computer-assisted AVR estimation system which uses VAMPIRE and the user interface tool we developed. Conclusions are given in Section 4.5.

4.2 Introduction

The arterio-venous ratio (AVR) is a medical measurement that is often used to quantify generalized retinal arteriolar narrowing [47]. Retinal arteriolar narrowing is a condition where retinal microvasculature changes due to chronically elevated blood pressure and other processes [78]. It has been found to have a link with hypertension, risk of diabetes mellitus, risk of coronary heart disease and cerebral atrophy [78, 79, 80, 8]. However, retinal arteriolar narrowing is difficult to quantify objectively through direct ophthalmoscopy and manual estimation. Hence, numerous researches have been done to

develop computer assisted AVR estimation with a standardized protocol. Semi-automated estimated AVR as a measure of generalized retinal arteriolar narrowing has been used in several studies such as the atherosclerosis risks in communities (ARIC) study [6, 81, 82], the Blue Mountains Eye Study[83, 84], and the Beaver Dam Eye Study[85, 86].

4.3 AVR estimation protocol

AVR is generally known as ratio of arteriole width to venular width. A study to compare different AVR calculation methods was done by Hemminski *et al* [48]. In their study, they compared four different formulae on both left and right eye. The formulae they used for comparison are;

i. central retinal arteriolar equivalent (CRAE)/ central retinal venular equivalent (CRVE);
ii. mean arteriole width/ mean venule width;
iii. sum of widths of arterioles/ sum of widths of venules;
iv. sum of squares of widths of arterioles/ sum of squares of widths of venules.

They found that AVR calculated by CRAE/CRVE has the best repeatability. In addition, there is no significant difference between CRAE/CRVE measurements taken from left eye and right eye [48, 76, 77]. This indicates the suitability of this formula to represent vascular changes in the eye of the patient. The central retinal arteriolar equivalent (CRAE) was first derived by Parr *et al* [5]. It is estimated from arteriolar widths around a predefined zone concentric with the optic disc. The zone is fixed to be 0.5DD to 1DD from optic disc margin. The zone (0.5DD-1DD) is chosen based on the data which showed that arteriolar widths appear to decrease significantly after this distance from the optic disk in patients with hypertension [47].

To obtain CRAE, paired vessels were combined to estimate trunk vessel, and then trunk vessels were combined iteratively until all vessels are combined into the summary

measure, CRAE. The formula used to calculate vessel trunk width from a vessel pair is shown as the following:

$$W_c = \sqrt{0.87W_a^2 + 1.01W_b^2 - 0.22W_aW_b - 10.76}$$

Where W_c= width of vessel trunk, W_a= width of smaller branch, W_b= width of larger branch.

Hubbard *et al* [75] later derived a corresponding formula for central retinal venular equivalent (CRVE):

$$W_c = \sqrt{0.72W_a^2 + 0.91W_b^2 + 450.05}$$

The final AVR is calculated as CRAE/CRVE.

The main shortcoming in Parr's method is that it requires a careful mapping of retinal vessels to trace vessel pairs, which is laborious and difficult [6]. Hence, Hubbard *et al* [6] further proposed a simplified version of the method which is less time consuming and correlates well with Parr's method [74]. However, this improvised method still has two main limitations [2]; it is dependent on scale because of the presence of coefficient in the formulae and it is affected by the number of vessels. Later, Knudtson *et al* [2] proposed an improvement of the method which addresses the limitations of the previous method. The formulae they proposed to calculate vessel trunk from vessel pair are:

$$W_A = \frac{1}{\sqrt{BCA}}\sqrt{W_1^2 + W_2^2}$$

$$W_V = \frac{1}{\sqrt{BCV}}\sqrt{W_1^2 + W_2^2}$$

Where *BCA*= branching coefficient of artery, *BCV*=branching coefficient of vein

W_A = width of artery trunk, W_V = width of vein trunk, W_1 = width of smaller branch, W_2 = width of larger trunk.

4.4 Computer-assisted AVR estimation

Computer-assisted AVR estimation can be categorized into semi-automatic [104, 105] and automatic system [8, 10, 11, 106]. The overall flow of the algorithm for automatic AVR estimation system is shown in Figure 4.1.

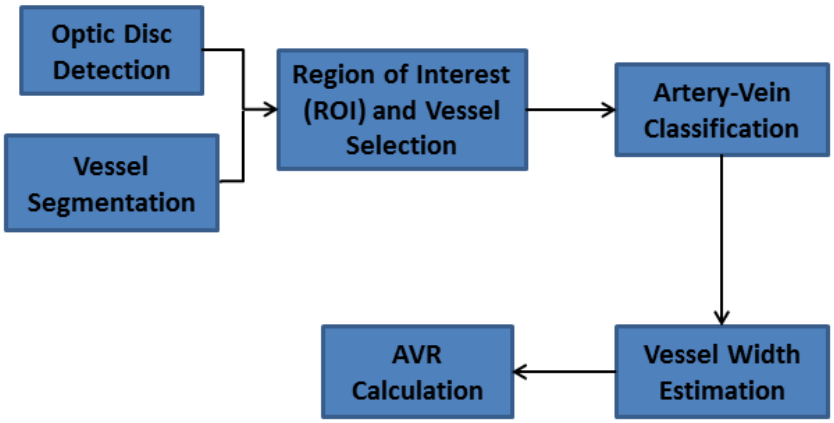

Figure 4.1: Overall algorithm flow for automatic estimation of AVR

Our implementation of computer-assisted AVR estimation is a semi-automatic one. We developed a user interface tool to enable clinicians to provide input manually ROI and vessel selection as well as artery-vein classification. Subsequently optic disc detection, vessel segmentation and vessel width estimation will be implemented with VAMPIRE. Figure 4.2 gives an illustration of our system.

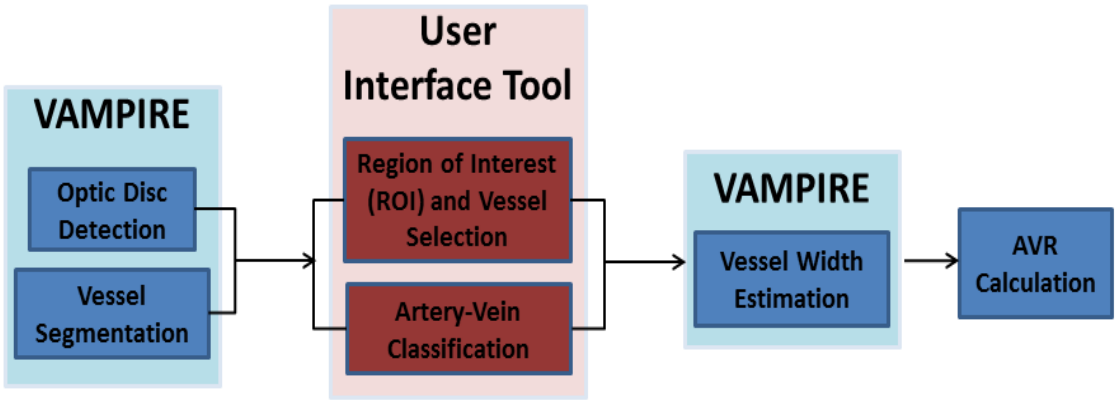

Figure 4.2: Our implementation of semi-automatic estimation of AVR. Blue box indicates automatic process whereas red box indicates manual process.

Our system has been used by ophthalmologists and geneticist to obtain AVR values for images acquired within the Tayside diabetic screening programme at Ninewells Hospital, Dundee, for correlational studies (i.e., to find correlation between AVR and cardiovascular disease).

4.4.1 User interface tool

This section describes the user interface tool used by clinicians to provide manual input on ROI and vessel selection, and in parallel, artery and vein labelling of each vessel. Below are brief instructions on how to use the tool.

User will first be prompted to enter name and session.

Figure 4.3: User interface tool stage 1

Click ‘Open Folder’ to choose folder containing images to process.

Figure 4.4: User interface tool stage 2

First; click around OD edges to define OD boundary.

Figure 4.5: User interface tool stage 3

An ellipse will be fitted to the points. Ellipse is fitted by the algorithm developed by Pilu et al [7].

Figure 4.6: User interface tool stage 4

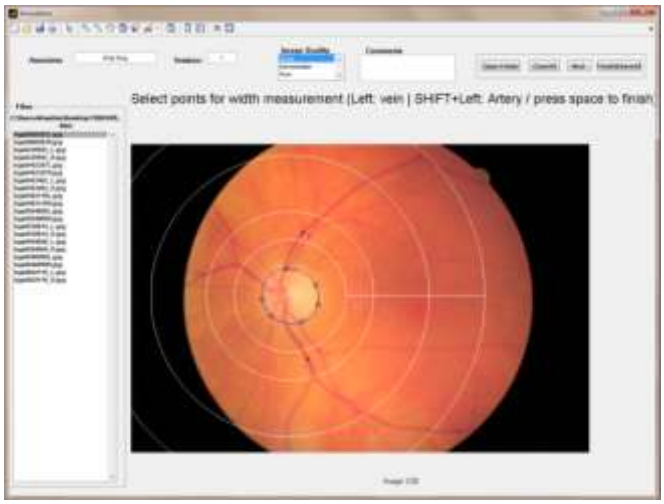

At this stage, user will select vessel of interest for calculation of AVR within the region of interest which is the second concentric zone (0.5DD-1DD). In parallel, users will also distinguish manually arteries from veins. Shown on the figure, vessel with red point represents artery whereas vessel with blue point represents vein.

Figure 4.7: User interface tool stage 5

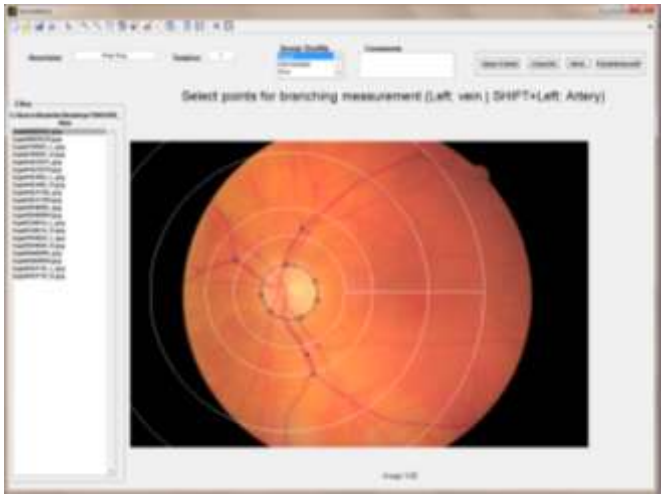

Third; User will select branching points for branching coefficient calculation which will be used as a parameter in the CRAE and CRVE formulae.

Figure 4.8: User interface tool stage 6

4.4.2 AVR calculation

We estimated the AVR value based on protocol devised by Knudtson *et al* [2], as discussed in Section 4.3. The CRAE and CRVE formula proposed by Knudtson *et al* require branching coefficients (BCA and BCV) as the parameter. To obtain these parameters, a subset of images (12 images) was processed to obtain branching coefficients of artery and vein branches using VAMPIRE. BCA value obtained for artery is 1.25(comparable to theoretical BC of 1.26 [46], and experimentally calculated arteriolar BC 1.28 [2]), and for vein is 1.17 (comparable to the experimentally calculated venular BC 1.11[2]). Upon obtaining the branching coefficient, CRAE and CRVE value and subsequently AVR value can be calculated for each image for clinical studies. Algorithm to calculate AVR is shown in the pseudo-code below:

Algorithm: To calculate AVR

Input: Vector ArteryW which contains all widths of selected arteries and Vector VeinW which contains all widths of selected veins.

Output: AVR

Sort ArteryW and VeinW in descending order

```
W2=ArteryW;
while |W2| ~= 1 do
   W1=W2;
   W2=[];
   while |W1| >1 do
         Select the thickest vessel and thinnest vessel from W1 and store
         BCA*sqrt(W1(1)^2 + W1(end)^2 in vector W2.
   end while

   if |W1|==1 then
      W2(a+1)=W1;
      W1=[];
   end if
end while
CRAE=W2;


W2=VeinW;
while |W2| ~= 1 do
   W1=W2;
   W2=[];
   while |W1| > 1 do
         Select the thickest vessel and thinnest vessel from W1 and store
         BCV*sqrt(W1(1)^2 + W1(end)^2 in vector W2.
   end while

   if |W1|==1 then
      W2(a+1)=W1;
      W1=[];
   end if
end while
CRVE=W2;

AVR=CRAE/CRVE;
```

4.5 Conclusion

In this chapter, we have introduced the method used to estimate arterio-venous ratio (AVR), a clinical measurement that is often linked to cardiovascular diseases. We have also demonstrated how we obtain AVR values semi-automatically from retinal images using VAMPIRE and the user interface tool we developed to obtain input from user manually. This system has been used by ophthalmologist and geneticist from Ninewells Hospital, Dundee to study the predictive power of AVR for cardiovascular diseases. In the next chapter, we will present an artery-vein classification framework in which we attempt to automate vessel selection and vessel classification which is currently done manually using the user interface tool presented in this chapter.

CHAPTER 5

ARTERY-VEIN CLASSIFICATION

5.1 About this chapter

In this chapter, we present a method for automatic artery-vein calculation. The region of interest for AVR calculation is set to be 0.5DD-1DD from optic disc margin, which follows the protocol by Knudtson *et al* [2]. Vessels are selected within this region based on the criteria that they are not crossing vessel and are of the suitable width. Each vessel is then compared to its nearest neighboring vessel. Comparison is done based on the mean of intensity value in the green channel. Initial experiment with 56 images (284 veins, 219 arteries) shows promising result (accuracy of 240/284 for vein and 201/219 for artery). This chapter is organized as follows. Section 5.2 introduces the motivation for artery-vein classification as well as the possible features that can be used for classification. Section 5.3 discusses about the related work in artery-vein classification. Section 5.4 presents the methodology of our algorithm. Section 5.5 discusses our result and finally the chapter is concluded in Section 5.6.

5.2 Introduction

In Chapter 4, we presented a user interface tool where the selection of arteries and veins, and artery-vein classification were done manually by user. In this chapter, we attempt to automate these two steps with the main focus on artery-vein classification. Arteries are blood vessels that carry oxygenated blood and veins are blood vessels that carry de-oxygenated blood. In fundus images, arteries generally appear to be brighter, thinner and larger ones have a stronger central reflex more often than veins. Apart from being an important step towards the automatic estimation of AVR, accurate categorization of arteries and veins is important from the medical point of view because

certain pathologies affect only either artery or vein [13]. Therefore, artery and vein classification is a basis for automated system to recognize these types of diseases by analyzing the different effect on arteries and veins individually. Here, we target only the classification of vessels for the purpose of AVR calculation. Although, in general, artery-vein classification is a difficult problem, our literature search reveals that arteries and veins can be distinguished from each other based on their appearance and structural pattern as listed below;

I. Appearance

i. Arteries tend to have smaller width than veins [104];

ii. Arteries tend to be brighter than veins [103, 12];

iii. Arteries tend to have stronger central light reflex than veins [11, 102];

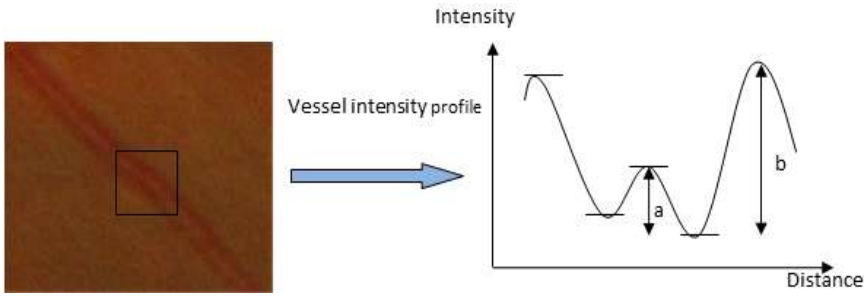

Figure 5.1: Vessel and its extracted intensity profile

The *central reflex coefficient* is a measurement of a vessel's central light reflex [11]. Figure 5.1 shows the intensity profile extracted from a vessel. The center peak is the reflection by the vessel, which is captured in the central reflex coefficient. The formula used to calculate this coefficient is $CRC = \frac{a}{b}$ where *a*=distance between central reflex and the lowest intensity of the profile, and *b*=distance between highest intensity and lowest intensity of the profile.

Figure 5.2: The figure shows two pairs of artery and vein cropped from a retina image. The artery can be recognized as having a brighter color, stronger central reflex on the centre, and being slightly thinner than vein.

iv. Arteries tend to be straighter whereas veins are more tortuous [102].

Tortuosity is a measure of retinal vessel morphology [38]. It is commonly defined as the integral of the curvature square along the path of the vessel, normalized by the total path length [38]. Example of tortuous and less tortuous vessels is shown in Figure 5.3. Tortuosity measure as a classification feature may not be a good choice. This is because, in a healthy eye, retinal blood vessels are straight or gently curved. However, in some diseased eyes, the blood vessels become tortuous, i.e. they become dilated. The tortuosity may be focal occurring only in a small region of retinal blood vessels, or it may involve the entire retinal vascular tree [36]. This will cause wrong identification of vessels type.

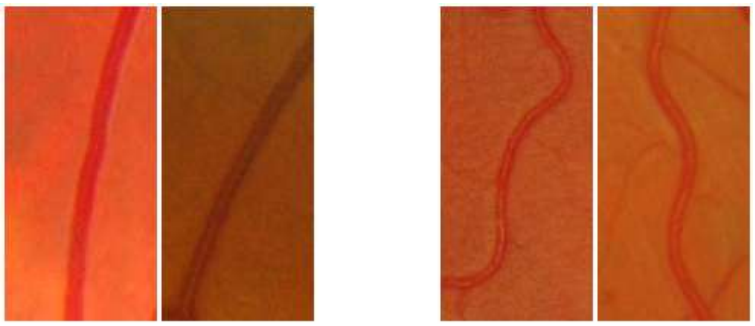

Figure 5.3: Left: two examples of less tortuous vessels. Right: two examples of more tortuous vessels.

II. Structural pattern

i. Arteries normally alternate with veins around the optic disc [8, 102];

ii. Arteries never cross arteries and veins never cross veins; if crossing occurs, the darker vessel is the vein and vice versa [13, 102].

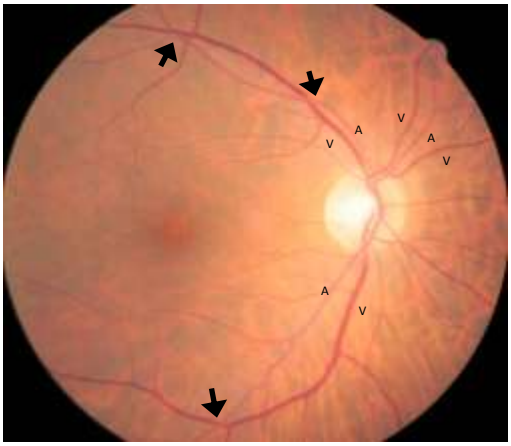

Figure 5.4: Illustrates the alternate pattern of arteries and veins. The arrows point to crossing site between vessels which involve an artery and a vein.

5.3 Related work

Several authors have used vessel appearance as their classification feature to classify vessels into arteries and veins. Ruggeri *et al* [33] used colour features such as variance of red channel and mean of hue value. However, they divided the image into four quadrants and classify the vessels separately in order to counter the effect of uneven illumination and contrast of the retina image. Tramontan *et al* [11] extended Ruggeri's work and used only central reflex as their classification feature in a different dataset. Muramatsu *et al* [10] used features from red, green, blue channels and contrast from each channels for their classifier. These authors reported promising results on their dataset suggesting that vessel appearance features are good classifiers of arteries and veins. However, one of the most common problems with using appearance is variability across images and subjects. This can be caused by differences in camera setting,

artifacts and difference in pigmentation of the retinal pigment epithelium below the blood vessels [8].

Kai Rothaus *et al* [13] applied only structural pattern of the vessel to classify arteries and veins. Their algorithm first detects vessel crossing and perform vessel labeling based on the fact that vessel crossing must involve one artery and one vein. Their classification algorithm does not only aim to classify vessels for large and well contrasted vessels for AVR calculation. It is able to classify the whole retinal vessel tree. The authors tested their algorithm using both ground truth vessel segmentation as well as automatically segmented vessel map using vessel segmentation algorithm by Soares *et al*. Automatically segmented vessel map, as expected, poses more problems to the algorithm due to the sometimes wrong and incomplete automatic segmentation of vessel which creates unconnected vessel segments. This method is highly dependent on the quality of segmented vessel map and even with user intervention and ground truth vessel map, classification of vessels using vessel crossing as criteria is often complicated and does not always produce satisfactory result.

Some authors combined appearance features with vessel tree structure. Niemeijer *et al* [8] used color features from red channel, green channel, hue and saturation to train their classifier. For final labelling of the vessels, they used the prior information that vein and artery always come in pair. Vàzquez *et al* [9] and Kondermann *et al* [12] used color features combined with vessel tracking in order to improve their classification result.

5.4 Methodology

5.4.1 Algorithm overview

Retina images were first pre-processed to correct uneven illumination using the algorithm developed by Foracchia *et al* [37]. Only the green channel is used for classification purpose because it has the best vessel contrast compared to other channels [15, 90, 91]. Optic disc detection and vessel segmentation is performed with VAMPIRE as explained in Section 2.6. First, we determine the region of interest for AVR calculation which is 0.5DD-1DD from optic disc margin. Then, vessels from this region are selected automatically in order to filter out unwanted vessels such as crossing vessels, combined vessels, and very thin vessels. The algorithm for vessel selection is explained in detail in Section 5.4.2. Next, we obtain mean of intensity value from the selected vessels. Each selected vessel is then classified by local comparison of intensity value with its nearest neighboring vessel. The overall algorithm is shown in Figure 5.5.

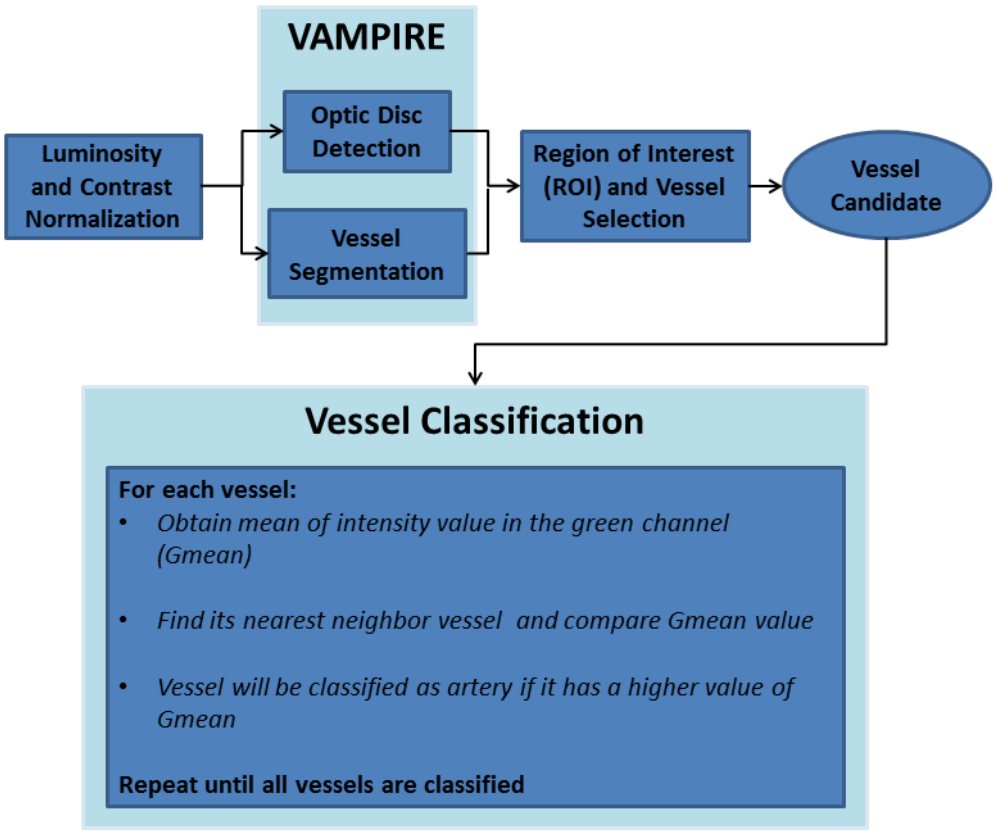

Figure 5.5: Flow diagram of our artery-vein classification framework.

5.4.2 Region of interest and vessel selection

First, the optic disc is located using the VAMPIRE software [1]. Then, a concentric region of interest is defined at 0.5DD to 1DD from the optic disc margin (refer to Figure 5.6). The region of interest is selected based on the protocol by Knudtson *et al* [2].

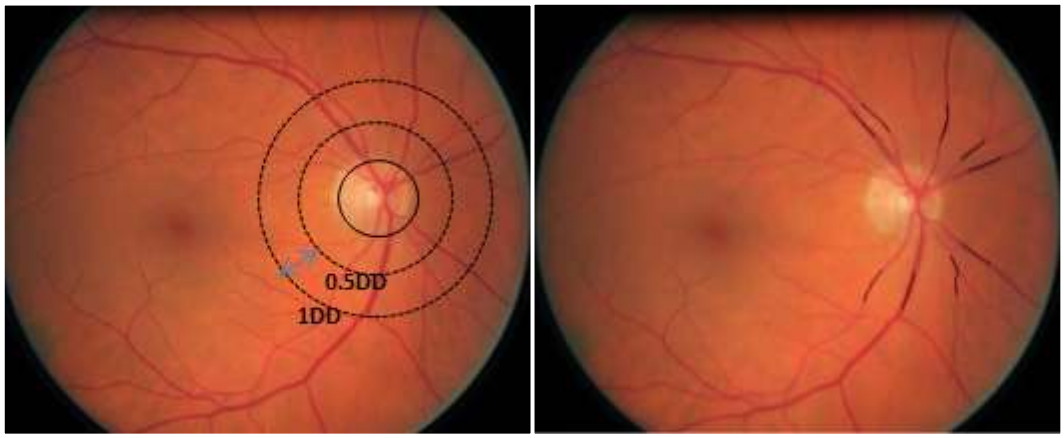

Figure 5.6: Left: Region of interest (0.5DD-1DD) Right: Selected vessels

Next, we proceed to choose vessels from this region of interest. The vessels are first segmented from the image and tracked using the VAMPIRE software [1]. All vessels that lie in the region of interest are chosen and then filtered to remove unwanted vessel. After filtering, the vessel candidates (Figure 5.5) will be classified as either artery or vein.

The types of unwanted vessels are listed below.

- Crossing vessels

  Sometimes a vessel may be detected wrongly at the crossing point between artery and vein. This 'crossing vessel' is not an actual vessel but wrongly detected as one. It lies between two junctions and branching angle at the junctions is less than 45° [102]. This occurs when the binary map is thinned to one pixel centerline using MATLAB's implementation of thinning algorithm [107]. The section where artery and vein cross becomes the centerline of a vessel fragment when the thinning algorithm is applied (Figure 5.5).

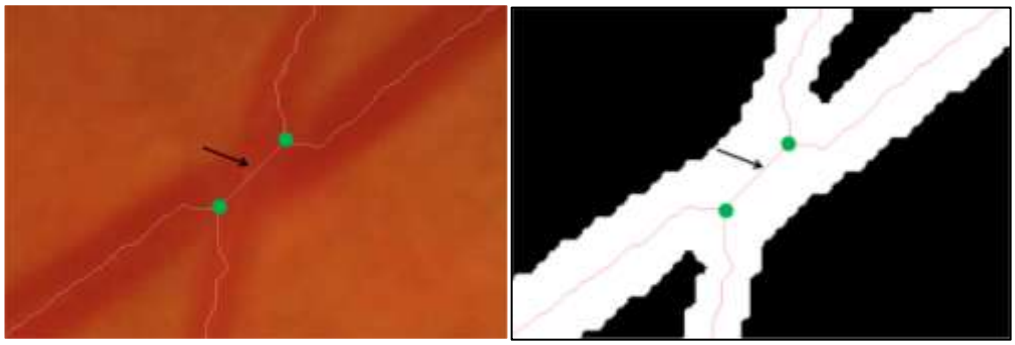

Figure 5.5: Left: Cropped image at vessel crossing. Right: Cropped binary vessel map at vessel crossing. The vessel pointed by the arrow is crossing vessel which resulted from the crossing of an artery and a vein (branching points shown in green circle).

Hence, our algorithm identifies this X shape crossing vessel by detecting vessel fragment that lies between two junction points and the branching angle at each junction is no more than 45°.

- Combined vessels

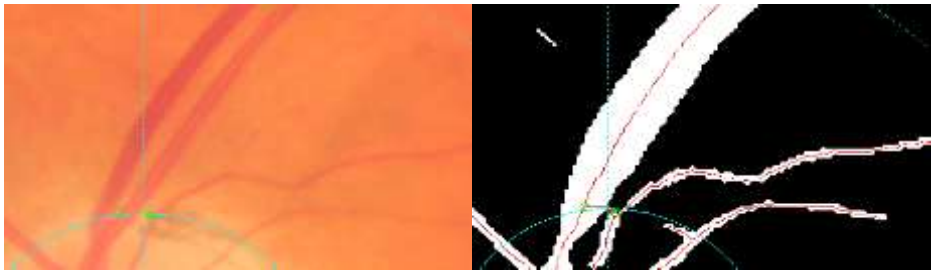

Figure 5.6: Left: original image of a vessel pair. Right: binary vessel map of the vessel pair.

Parallel vessels that are too close to each other may be falsely segmented as one vessel. In Figure 5.6, original image shows a pair of parallel vessels, one vein and another artery. However in the binary vessel segmentation map, they are detected as one large vessel. This type of vessel will be excluded from the final selection of vessels for AVR calculation. The algorithm to implement this is shown below.

Algorithm: To exclude combined parallel vessels

Input: Tree structure, Width: vector vessel width,

Output: Updated tree structure

Sort vector Width in descending order.

W = average of 3rd largest vessel and 4th largest vessel in the vector of vessel width

for v=1:tree.numVessels

if vessel is within region && vessel width/W>=1.5 **then**

Exclude this vessel from candidate vessel;

end if

end for

- Very thin vessel

For AVR calculation, vessels that are too small are excluded. This is because small vessels usually have poorer border contrast (Figure 5.7), and this will affect vessel width calculation which will subsequently affect the final AVR value. To do this, vessels with width that is less than 50% of the largest vessel in the region of interest will be excluded from the final selection.

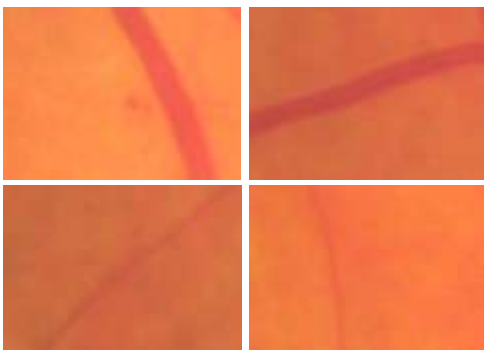

Figure 5.7: First row: thick vessels showing better contrast on vessel edge. Second row: thin vessel showing very poor contrast on vessel edge.

5.4.3 Classification features

As explained in Section 5.3, the appearance of retinal vessels such as color, brightness, central reflex, and width changes with location within the same image as well as across different images.

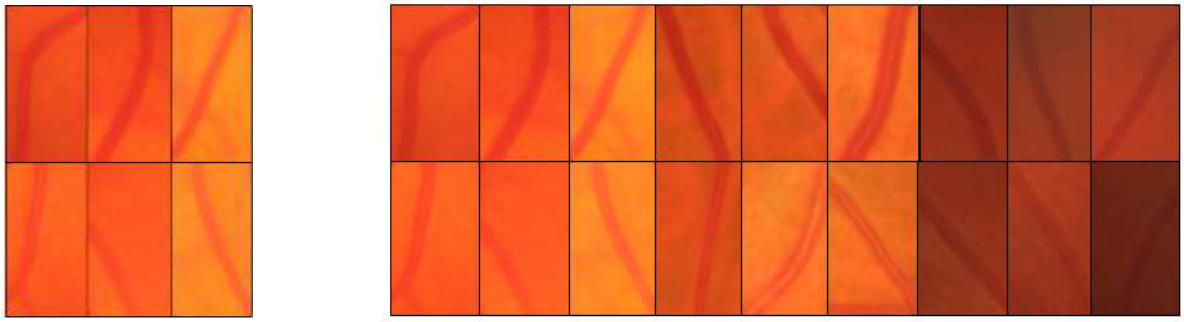

(a) (b)

Figure 5.8: (a) 1st row; veins from the same image. 2nd row; arteries from the same image

(b) 1st row: veins from different images. 2nd row: arteries from different images.

Figure 5.8 shows the appearance variation of artery and vein segments taken from different areas within the same image (Figure 5.8(a)) and across different images (Figure 5.8(b)). We can see that, arteries and veins do not show very much difference in terms of their appearance such as color, central reflex and width. We cannot claim that veins always have darker color, small central reflex and larger width. This is because there are also brighter, smaller veins or veins with larger central reflex. This can be seen clearly in Figure 5.8 where vessel segments were taken from different images as well as from different areas within the same image. Hence, from this observation, we can safely assume that almost none of the vessel's appearance (color, width, central reflex) feature for discrimination is globally valid. However, if classification is done locally, the discriminative power of vessel appearance features increases. Figure 5.9 illustrates this statement.

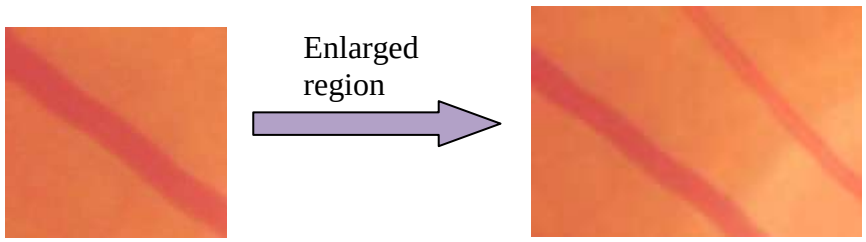

Figure 5.9: (a) Single vessel (b) Vessel with its nearest vessel

When given a single vessel, it is often impossible to recognize it as either an artery or vein just by looking at its appearance. However, when the region is enlarged to include its nearest neighboring vessel, the vessel can often be recognized as a vein by comparing their appearance (darker, larger width, less central reflex). Therefore, vessel appearance is only meaningful if it is not taken as an absolute value, but as a comparative value (e.g, darker in color). In this algorithm, we compare each vessel to its nearest neighboring vessel. To compare neighboring vessels, we chose the mean of the intensity in the green channel. The green channel is chosen because it shows the best contrast between arteries and veins compared to the red and blue channel.

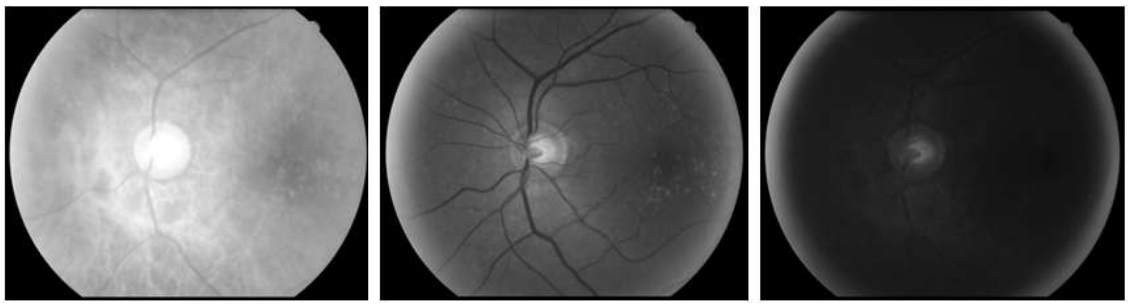

Figure 5.10: Figure shows the 3 channels of a color fundus image. From left: Red channel, Green channel and Blue channel

Henceforth, the mean of the intensity in green channel will be denoted as Gmean.

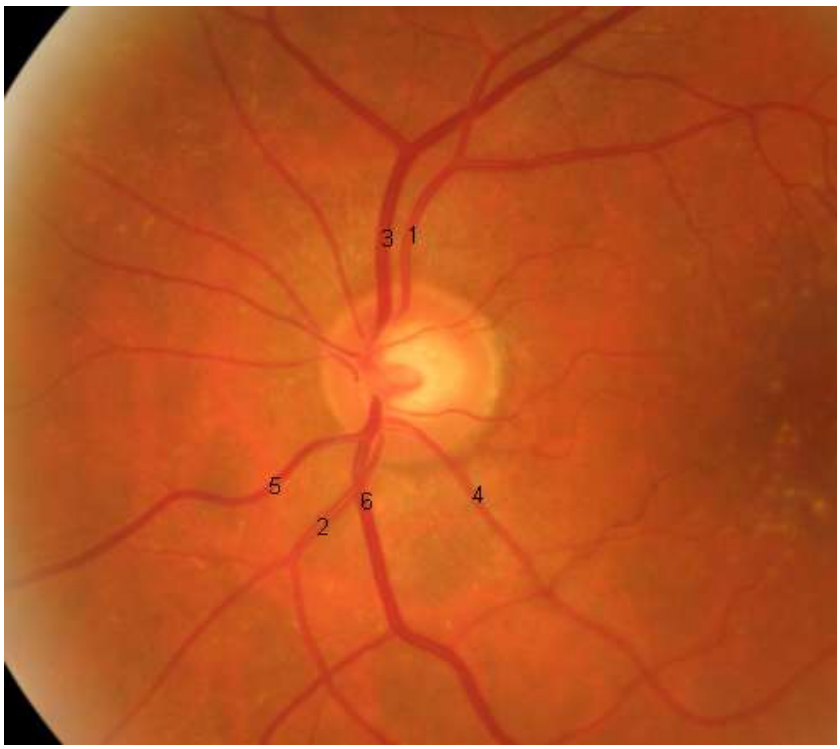

Figure 5.11: Retina image showing vessels chosen by the algorithm and the number attached to the vessel indicated the order of magnitude of mean of green channel value.

Figure 5.11 shows vessels that were selected automatically by our vessel selection algorithm, described in detail in Section 5.4.2. The number attached to the vessel is the order of magnitude of mean intensity value, (i.e., '1' indicates the highest Gmean value and '6' indicates the lowest Gmean value for this image). Artery should have a higher value of Gmean compared to vein because it is brighter. The next section will explain how the nearest neighboring vessel is chosen for each vessel as well as the method to classify the vessels into arteries and veins.

5.4.4 Classification method

This section shows step by step how our vessel classification algorithm is implemented starting from vessel selection to artery-vein classification. The overall flow of the algorithm can be seen in Figure 5.5.

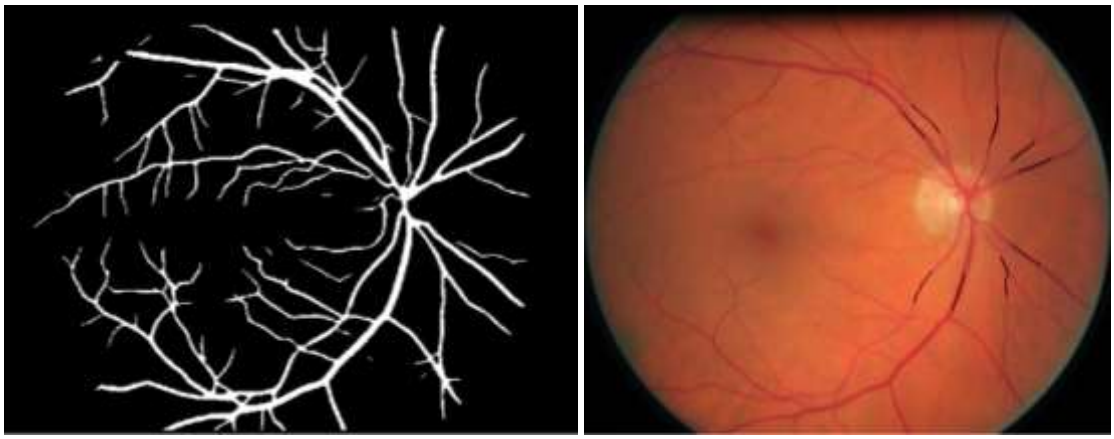

Figure 5.12: Left: binary vessel map of the image. Right: Image with the selected vessels in black

After vessel segmentation and optic disc detection, the region of interest (0.5DD-1DD) was defined. Then, vessel candidates were chosen using method described in Section 5.4.2. Figure 5.12 shows the vessel candidates for the image, which are selected by our algorithm. Then, starting from the centerline of each vessel, all vessel pixels that lie within 80% of vessel width and within the region of interest (0.5DD-1DD) are included in the calculation of Gmean for that vessel. The reason only vessel pixels that lie within 80% of vessel width are chosen is to ensure that no non-vessel pixels are included in the calculation of Gmean.

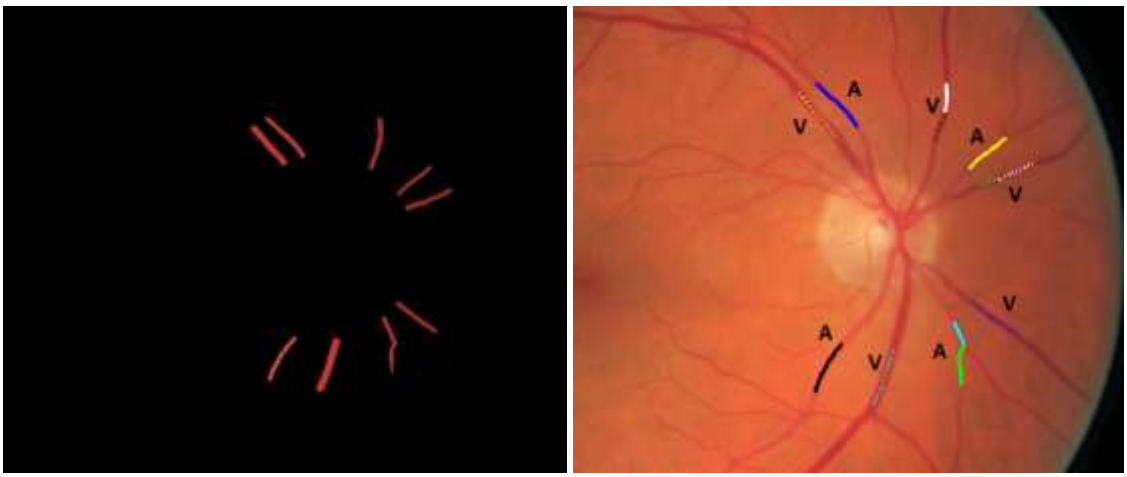

Figure 5.13: Left: The cropped region for each selected vessel where mean of green channel will be calculated. Right: : Vessel candidates with calculated Gmean, represented in colors; (black, blue, cyan, green, yellow, white, dotted black, dotted blue, dotted green, dotted yellow, dotted white) in the order of decreasing Gmean magnitude.

Next, for each of the vessel candidate, its nearest vessel is found. The nearest vessel is found by searching for the vessel with the smallest angular disparity centered on the optic disc as shown in Figure 5.14.

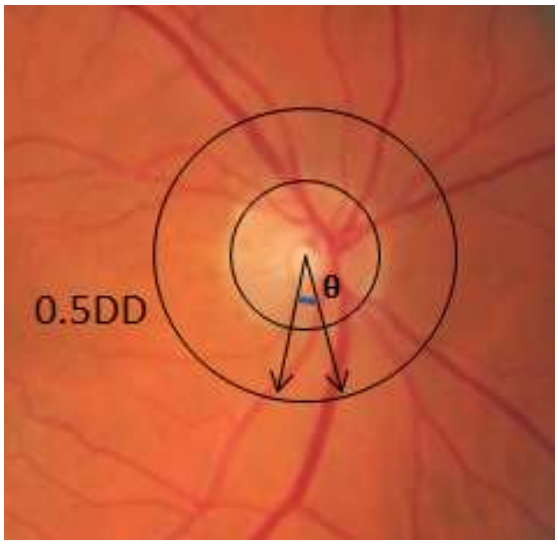

Figure 5.14: Illustration of how nearest vessel is found for every vessel candidate.

Each vessel is compared to its nearest vessel by Gmean. The vessel with higher value of Gmean (brighter) is classified as the artery.

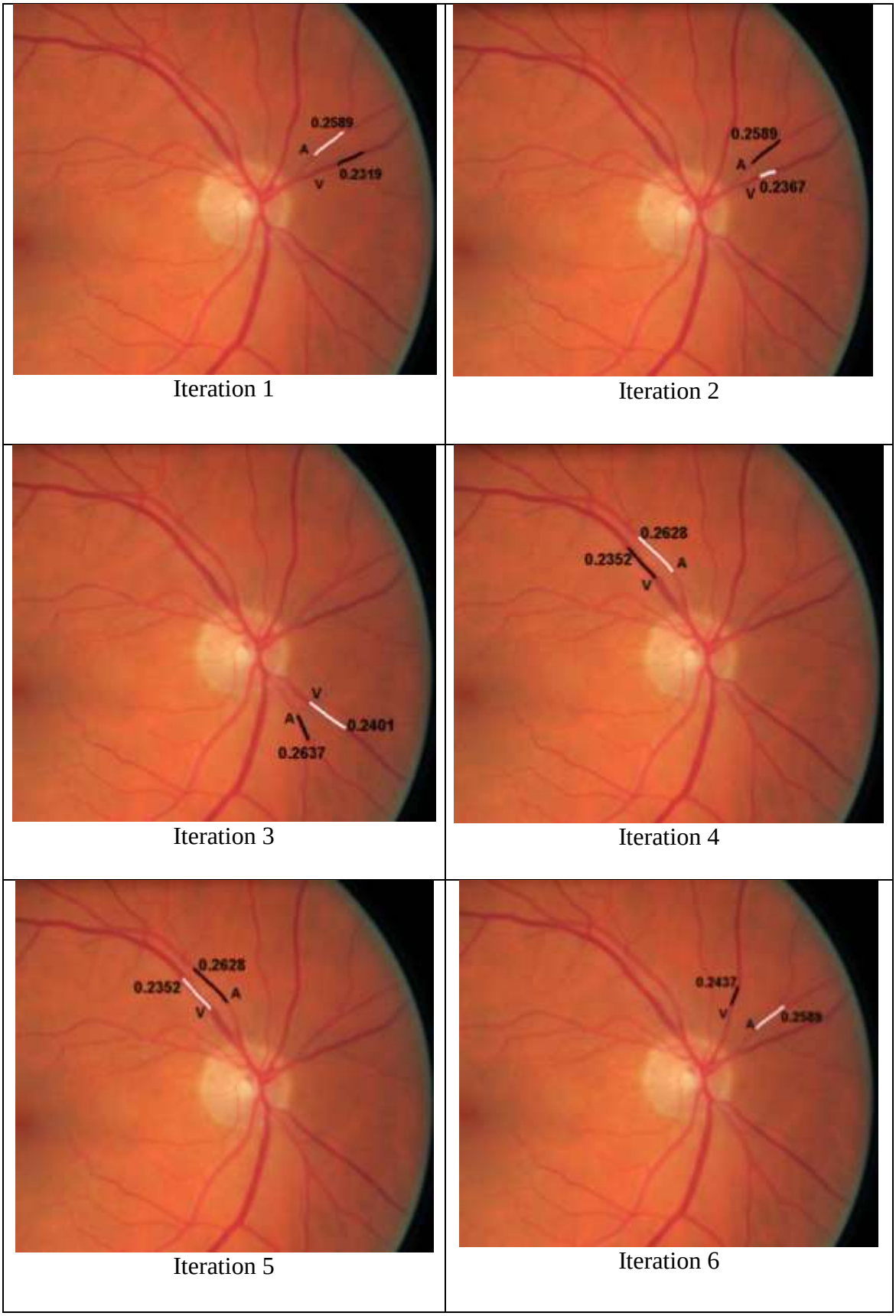

Figure 5.15: Shows the first 6 iterations of the vessel pairing. Vessel selected (in black), its nearest neighbour vessel (in white). Vessel label is shown where V=vein, A=artery. The number beside each vessel shows the Gmean value. Artery should have a higher Gmean.

Figure 5.15 shows the first 6 iterations of vessel pairing. The number of iteration equals to the total number of vessel candidates. Each vessel candidate will be paired with its nearest neighbour vessel and vessel classification will be done by comparing the Gmean value. The final result of algorithm on this image is shown in Figure 5.16.

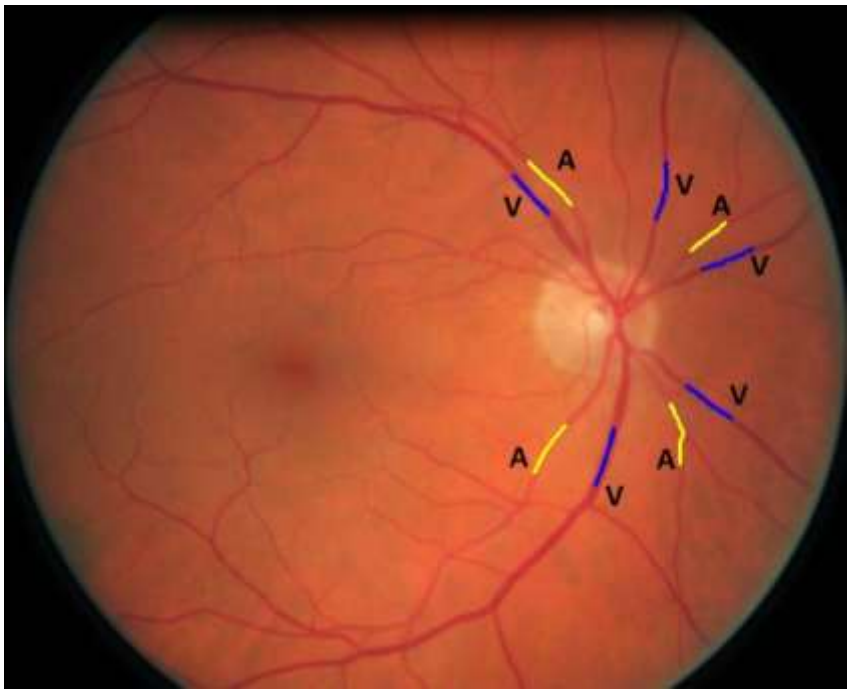

Figure 5.16: Final result (blue indicates vein and yellow indicates artery). The label beside each vessel is the ground truth label (A=artery, V=vein)

5.5 Experimental result

5.5.1 Materials

To test our algorithm we used 56 color fundus images obtained from the TENOVUS data set (Section 1.4). All images we used are of high resolution, 2336x3504 and are of good quality in terms of clarity and vessel contrast. From the 56 images, a total of 503 vessels (284 veins, 219 arteries) were classified. Vessels were automatically chosen by our vessel selection algorithm.

5.5.2 Result and discussion

From the experiment result, 240 veins were correctly classified out of 284 veins and 201 arteries were correctly classified out of 219 arteries. An illustration of the result of the algorithm is shown in Figure 5.17.

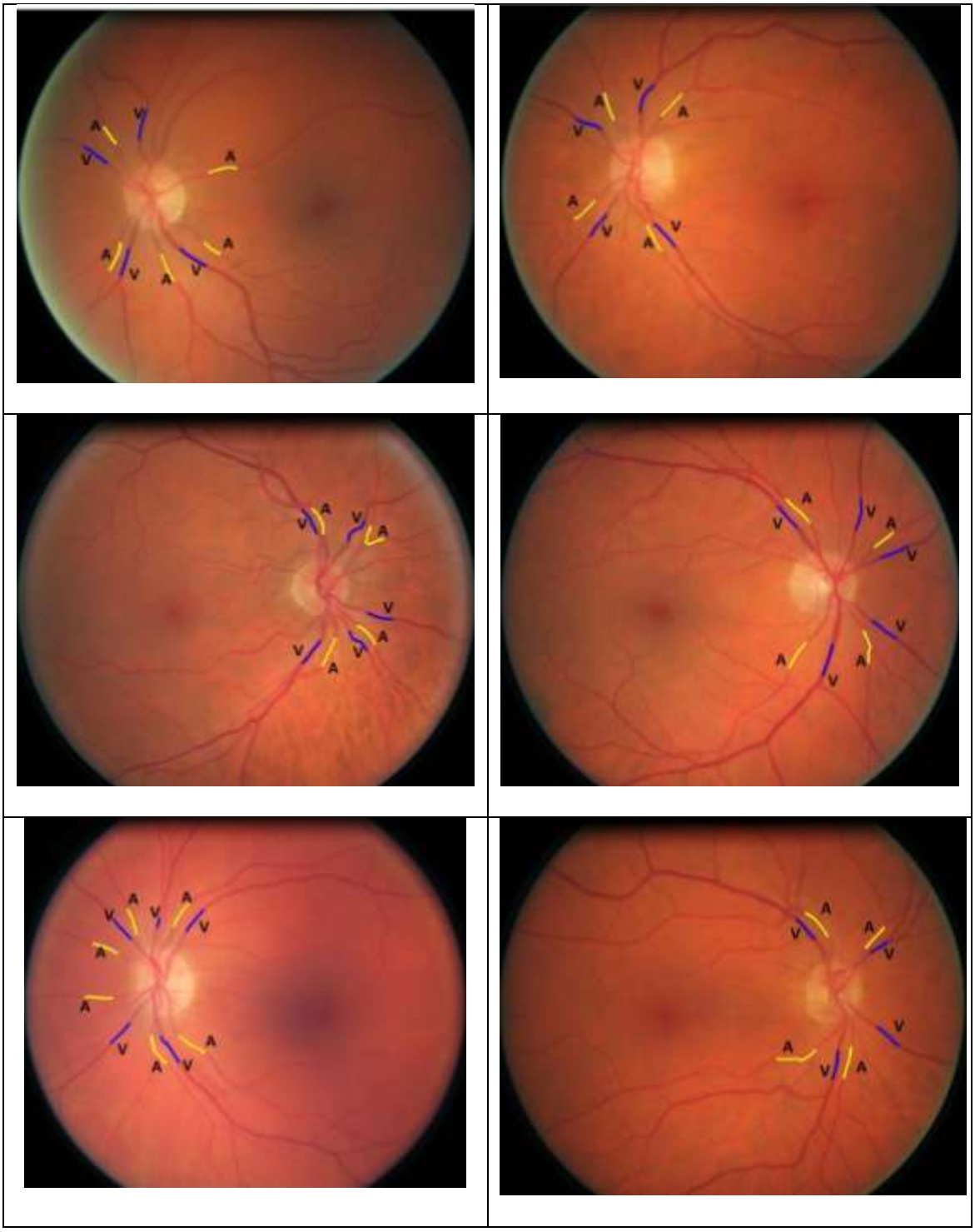

Figure 5.17: Experimental result (blue indicates vein and yellow indicates artery). The label beside each vessel is the ground truth label (A=artery, V=vein)

The algorithm works well if the vessels are properly segmented and if there are not many vessel crossings and vessel fragments in the region of interest. The failure of this algorithm is mainly due to over-fragmented vessel.

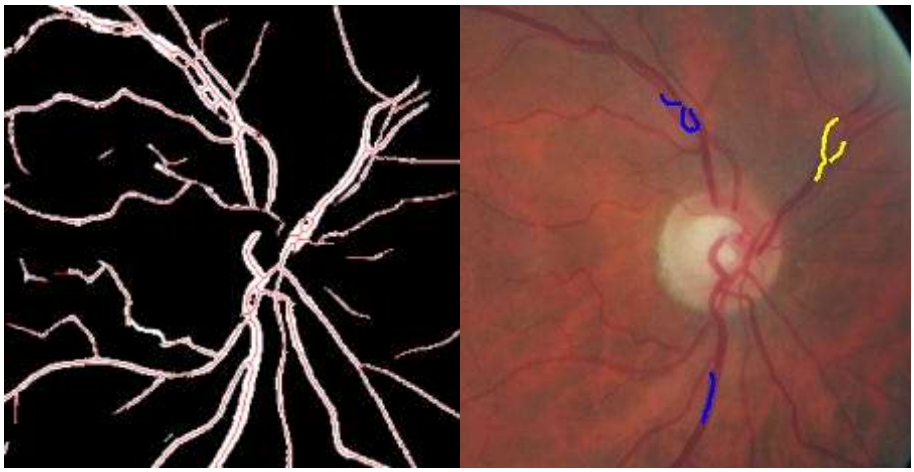

Figure 5.18: An example of wrong result caused by fragmented vessel. Left: binary vessel map Right: Color fundus image showing result of the algorithm.

Figure 5.18 shows an example of wrong result of this algorithm. As can be seen from the figure, the chosen vessels are fragments of an actual vessel. Hence, when pairing algorithm tries to pair up the fragments with its nearest neighbour vessel, the wrong vessel or vessel fragment will be chosen and hence, producing the wrong result. Moreover, the current algorithm uses threshold to filter out combined vessel and vessels that are too thin (Section 5.4.2). This works well when there is not much variation in the vessel widths as can be seen in the result displayed in Figure 5.17. However, when vessel widths vary a lot due to pathologies, the vessel selection algorithm discussed in Section 5.4.2 is not so effective. Hence, a possible future direction to improve this algorithm is to develop a more effective algorithm to filter out wrongly segmented vessel fragments and minimize the use of threshold in selecting vessel candidates for artery-vein classification.

5.6 Conclusion

In this chapter, we presented an automatic artery-vein classification algorithm. Vessel candidates which will be classified were carefully selected to exclude unwanted vessels such as crossing vessels, combined vessels and thin and low contrasted vessels. Each vessel was then classified based on the color feature taken from the green channel, Gmean. Classification was done locally by comparing each vessel candidate with its nearest neighboring vessel. The aim of local classification is to solve the problem of wide global variation of vessel appearance. A pilot experiment was done with 56 images (284 veins, 219 arteries). Result shows 240 veins were correctly classified out of 284 veins and 201 arteries were correctly classified out of 219 arteries. The algorithm is a potentially effective method for artery-vein classification. However, it also faces the same problem as Kai Rothaus *et al* [13] in that it is dependent on the quality of segmented vessel map. Any missing or wrongly detected vessel segment will result in erroneous vessel classification. Therefore, the possible future directions to improve this algorithm is to improve on the quality of vessel segmentation as well as improving the algorithm used to select proper vessel candidates for artery-vein classification.

CHAPTER 6

CONCLUSION

6.1 About this chapter

In this chapter, we review and summarize the work presented in this thesis. This chapter is organized as follows. Section 6.2 summarizes the main conclusion of experiment as well as the future direction for macula detection. Section 6.3 summarizes the AVR estimation system developed in our team and finally Section 6.4 summarizes the conclusion of experiment as well as future direction for artery-vein classification.

6.2 Fovea detection

In Chapter 3, we have presented an automated fovea detection algorithm. Our algorithm avoided the use of fovea appearance due to the wide variation of macula-fovea appearance especially in diseased images. The detection algorithm models the fovea region as an avascular based on anatomical information. Search region was defined based on anatomical priors; lies within main arcade, lies within a certain range of DM:DD and lies below the upper boundary of optic disc. We obtained the range of DM:DD from a sample data of 126 images, in contrast to common practice where DM:DD is often fixed as a constant (2DD or 2.5DD). Result was compared to annotation by two annotators. We tested our algorithm on 116 images of high resolution and of different qualities (good, medium and difficult). The best result reported from this algorithm was 73.3% (with the criteria that detected fovea center lies within 0.25DD of ground truth fovea center) and 87% (with the criteria that the detected fovea center lies within 0.5DD of ground truth fovea center). The main limitation of this algorithm is that it is dependent on the quality of vessel segmentation. Therefore, a clear future direction is to improve the vessel segmentation.

6.3 Tool for arterio-venous ratio (AVR) estimation

In Chapter 4, we have presented the semi-automated AVR estimation system developed in our team. This system is a combination of VAMPIRE and a user interface tool develop by the author to obtain manual input from user. The users of this system are the clinicians from Ninewells Hospital, Dundee to aid their clinical research of the relation of AVR with cardiovascular diseases as well as other pathologies. Future work should make this system a fully automated one, where automatic artery-vein classification plays an important part. Our work in artery-vein classification was presented in Chapter 5.

6.4 Artery-vein classification

In Chapter 5, we have presented an automated artery-vein classification algorithm in an attempt to fully automate the semi-automated AVR estimation system presented in Chapter 4. Instead of using vessel color as an absolute feature we used the color information as a comparative feature, where we compared each vessel to its nearest neighbouring vessel and classify the brighter vessel as the artery. We tested our algorithm on 56 (284 veins, 219 arteries) good quality images of high resolution. The result was, 240 veins were correctly classified out of 284 veins and 201 arteries were correctly classified out of 219 arteries. The main limitation of this algorithm is that because vessels are classified by comparing with the nearest neighbouring vessel, selection of wrong neighbouring vessel will result in erroneous classification. This often occurs when vessels are severely fragmented or wrong detection of vessel. Moreover, the algorithm used to filter out very thin vessels was based on threshold, which is not ideal. Therefore, a possible future direction to improve our method is to develop a more effective vessel selection algorithm as well as to improve the quality of vessel segmentation.

BIBLIOGRAPHY

[1] A.P. Rovira, T.McGillivray, E Trucco, K S Chin, K Zutis, C Lupascu, D Tegolo, A Giachetti, PJ Wilson, A Doney, B Dhillon. VAMPIRE: Vessel Assessment and Measurement Platform for Images of the Retina. *Proc IEEE Int Symp on Engineering in Biology and Medicine*, Boston, Aug-Sep 2011.

[2] M.D.Knudtson, K. Lee, L.D. Hubbard, T.Y. Wong, R.Klein, B.E.K. Klein. Revised formulas for summarizing retinal vessel diameters. *Current Eye Research*, 27(3):143-9, 2003.

[3] MESSIDOR: Methods for Evaluating Segmentation and Indexing techniques Dedicated to Retinal Ophthalmology http://messidor.crihan.fr/download.php

[4] J.V.B. Soares, J.J. G. Leandro, R. M. Cesar Jr., Herbert F. Jelinek, M.J. Cree. Retinal Vessel Segmentation Using the 2-D Gabor Wavelet and Supervised Classification. *IEEE Transactions on Medical Imaging*, Vol.25, No.9, September 2009.

[5] J.C Parr, GFS Spears. Mathematic relationships between the width of a retinal artery and the widths of its branches. *Am J Ophthalmol*, 77:478–83, 1974.

[6] L.D Hubbard, R.J Brothers, WN King, LX Clegg, R. Klein, L.S Cooper, A.R Sharrett, M.D Davis, J. Cai. Methods for evaluation of retinal microvascular abnormalities associated with hypertension/sclerosis in the Atherosclerosis Risk in Communities(ARIC) study. *Opthalmology*.106:2269-2280; 1999.

[7] M. Pilu, A. Ftzgibbon. Direct Least Squares Fitting of Ellipses. http://homepages.inf.ed.ac.uk/rbf/CVonline/LOCAL_COPIES/PILU1/demo.html

[8] M. Niemeijer, X. Xu, A.V. Dumitrescu, P. Gupta, B.Ginneken, J.C. Folk, M.D. Abramoff. Automated Measurement of the Arteriolar-To-Venular Width Ratio in Digital Color Fundus Photographs. *IEEE Transactions On Medical Imaging*, vol.30, no.11, November 2011.

[9] S.G. Vàzquez, B. Cancela, N. Barreira, M. G. Penedo, M. Saez. On the Automatic Computation of the Arterio-Venous Ratio in Retinal Images: Using Minimal Paths for the Artery/Vein Classification. *Digital Image Computing: Techniques and Applications*, 2010.

[10] C. Muramatsu, Y. Hatanaka, T. Iwase, T. Hara, H. Fujita. Automated selection of major arteries and veins for measurement of arteriolar-to-venular diameter ratio on retinal fundus images. *Computerized Medical Imaging and Graphics* 35,472– 480, 2011

[11] L. Tramontan, E. Grisan, A. Ruggeri. An improved system for the automatic estimation of the Arteriolar-to-Venular diameter Ratio (AVR) in retinal images. *IEEE EMBS Conference Vancouver*, British Columbia, Canada, August 20-24, 2008.

[12] C. Kondermann, D. Kondermann, M. Yan. Blood Vessel Classification into Arteries and Veins in Retinal Images. *Proc. SPIE*, 2007.

[13] K. Rothaus, P. Rhiem, and X. Jiang. Separation of the Retinal Vascular Graph in Arteries and Veins. *Springer-Verlag Berlin Heidelberg*, pp. 251–262, 2007.

[14] E. Grisan and A. Ruggeri. A divide et impera strategy for automatic classification of retinal vessels into arteries and veins. *Proceedings of the 25Ih Annual International Conference of the IEEE EMBS*, 2003

[15] J.V.B. Soares, J.J. G. Leandro, R. M. Cesar Jr., Herbert F. Jelinek, M.J. Cree. Retinal Vessel Segmentation Using the 2-D Gabor Wavelet and Supervised Classification. *IEEE Transactions on Medical Imaging*, Vol.25, No.9, September 2009.

[16] A. Giachetti, K.S Chin, E.Trucco, C. Cobb, P. J Wilson. Multiresolution localization and segmentation of the optical disc in fundus images using inpainted background and vessel information. *Proc. 18th IEEE Intl Conf on Image Processing*, Brussels, Sep 2011.

[17] A.Perez-Rovira,E. Trucco. Contextual optic disc location in retinal fundus images. *Journal of Modern Optics,* Vol.57 Issue 2, Pp. 136-144, 2010.

[18] C. Sinthanayothin, J. F Boyce, H. L Cook, T. H Williamson. Automated localisation of the optic disc, fovea, and retinal blood vessels from digital colour fundus images. *Br J Ophthalmol,* vol 83, pp 902–910, 1999.

[19] H. Li, and O. Chutatape. Automated Feature Extraction in Color Retinal Images by a Model Based Approach. *IEEE Transactions on Biomedical Engineeering,* Vol.51, No.2, February 2004.

[20] O. Chutatape. Fundus Foveal Localization Based on Vessel Model. *Proceedings of the 28th IEEE EMBS Annual International Conference*, New York City, USA, Aug 30-Sept 3, 2006.

[21] H. Ying, J.C.Liu. Automated Localization of Macula-Fovea Area on Retina Images Using Blood Vessel Network Topology. *ICASSP,* Pp 650 – 653, 2010.

[22] R.T. Smith, J.K. Chan, T. Nagasaki, U.F. Ahmad, I. Barbazetto, J. Sparrow, M. Figueroa, J. Merriam. Automated Detection of Macular Drusen Using Geometric Background Leveling and Threshold Selection. *Arch Ophthalmol,* Vol. 123, Feb 2005.

[23] N.M. Tan, D.W.K. Wong, J. Liu, W.J. Ng, Z. Zhang, J.H. Lim, Z. Tan, Y. Tang, H. Li, S. Lu, T.Y. Wong. Automatic Detection of the Macula in the Retinal Fundus Image by Detecting Regions with Low Pixel Intensity. *Proc. ICBPE*, pp 1-5, 2009.

[24] K. W. Tobin, E.Chaum, V. Priya Govindasamy, T. P. Karnowski. Detection of Anatomic Structures in Human Retinal Imagery. *IEEE Transactions on Medical Imaging*, Vol.26, No.12, December 2007.

[25] Z .Liang, D. W.K. Wong, J. Liu, K.L Chan, T.Y Wong. Towards automatic detection of age-related macular degeneration in retinal fundus images. *32nd Annual International Conference of the IEEE EMBS*, Buenos Aires, Argentina, August 31 - September 4, 2010.

[26] J.M Provis, P.L. Penfold, E.E. Cornish, T. M Sandercoe, M.C Madigan. Anatomy and development of the macula: specialization and the vulnerability to macular degeneration. *Clinical and Experimental Optometry*, 88:5:269-281, 2005.

[27] K. Rohrschneider. Determination of the location of the fovea on the fundus. *IOVS*, Vol.45, No.9, September 2004.

[28] K.H Mok, V.W.H Lee. Disc –to-Macula Distance to Disc-Diameter ratio for Optic Disc Size Estimation. *Journal of Glaucoma*, 11:392-395, April 4, 2002.

[29] H.W.Larsen, The Ocular Fundus: a Color Atlas, 1976.

[30] D.B. Barr, C.R. Weir, A.T.Purdie. An appraisal of the disc-macula distance to disc diameter ratio in the assessment of optic disc size. *Ophthal. Physiol*. Opt. Vol.19, No. 5, pp. 365-375, 1999.

[31] J. D'Errico, http://www.mathworks.com/matlabcentral/fileexchange/8277.

[32] I. J. Deary, A. J. Gow, M. D. Taylor, J. Corley, C. Brett, V. Wilson, H. Campbell, L. J. Whalley, P. M Visscher, D. J Porteous, J.M. Starr. The Lothian Birth Cohort 1936: a study to examine influences on cognitive ageing from age 11 to age 70 and beyond. *BMC Geriatrics*, vol. 7, pp. 28-40, 2007.

[33] E. Grisan and A. Ruggeri. A divide et impera strategy for automatic classification of retinal vessels into arteries and veins. *Proceedings of the 25Ih Annual International Conference of the IEEE EMBS*, 2003.

[34] H.F Jelinek, M.J. Cree. Automated image detection of retinal pathology.CRC Press, 2010.

[35] A. Perez-Rovira, E. Trucco. Robust optic disc location via combination of weak detectors. *30th Annual International IEEE EMBS Conference* pp.3542-3545. Columbia, Canada, 20-24 August, 2008.

[36] W.E.Hart, M.Goldbaum, B. Coˆte´, P.Kube, M. R.Nelson. Measurement and classification of retinal vascular tortuosity. *International Journal of Medical Informatics* 53, 239–252, 1999.

[37] M.Foracchia, E.Grisan. Luminosity and contrast normalization in retinal images. *Medial Image Analysis*, Vol. 8, Issue 3, pp 179-190, 2004.

[38] Y.L Cheung, Y.F. Zheng, W. Hsu, M.L Lee, Q.F. Lau, P. Mitchell, J.J. Wang,R. Klein, T.Y. Wong. Retinal Vascular Tortuosity, Blood Pressure, and Cardiovascular Risk Factors. *American Academy of Ophthalmology*, 118:812–818, 2011.

[39] J.S Wolffsohn, G.A Napper, S.M Ho, et al. Improving the description of the retinal vasculature and patient history taking for monitoring systemic hypertension. *Ophthalmic Physiol* Opt;21:441–9, 2011.

[40] International Committee for the Classification of Retinopathy of Prematurity. The International Classification of Retinopathy of Prematurity revisited. *Arch Ophthalmol* 123: 991–9, 2005.

[41] M.I Boone, M.E Farber, L. Jovanovic-Peterson, C.M Peterson. Increased retinal vascular tortuosity in gestational diabetes mellitus. *Ophthalmology* 96:251– 4, 1989.

[42] I. Tsui, K. Shamsa, J.K Perloff, et al. Retinal vascular patterns in adults with cyanotic congenital heart disease. *Semin Ophthalmol*, 24:262–5, 2009.

[43] D.C. Ferrara, H. Koizumi, R.F Spaide. Early bevacizumab treatment of central retinal vein occlusion. *Am J Ophthalmol* 144:864 –71, 2007.

[44] C. Orssaud, J. Dufier, D. Germain. Ocular manifestations in Fabry disease: a survey of 32 hemizygous male patients. *Ophthalmic Genet* 24:129 –39, 2003.

[45] N. Patton, T. Aslam, T. MacGillivray et al. Asymmetry of Retinal Arteriolar Branch Widths at Junctions Affects Ability of Formulae to Predict Trunk Arteriolar Widths. *IOVS*, vol. 47, no.4, April 2006.

[46] C. Murray. The physiological principle of minimum work 1. The vascular system and the cost of blood volume. *Proc Natl Acad Sci USA.* 12:207–214, 1926.

[47] T.Y Wong, R. Klein, B.E.K Klein, et al. Retinal microvascular abnormalities and their relationship with hypertension, cardiovascular diseases and mortality. *Surv Ophthalmol* 46:59–80, 2001.

[48] V. Hemminki, M.Kähönen , M.T.Tuomisto et al. Determination of retinal blood vessel diameters and arteriovenous ratios in systemic hypertension: comparison of different calculation formulae. *Graefe's Arch Clin Exp Ophthalmol* 245:8–17, 2007.

[49] MESSIDOR: Methods to evaluate segmentation and indexing techniques in the field of retinal ophthalmology; http://messidor.crihan.fr/description-en.php

[50] National Eye Institue of the NIH;
http://www.nei.nih.gov/photo/eyedis/images/EDA22_72.jpg

[51] S.S.Tiew, A.Perez-Rovirez, E. Trucco, S. Mahmood, P. Bishop, T. M. Aslam. Experience In Using The Vampire Retinal Analysis Tool To Assess Tortuosity In Patients Undergoing Bevacizumab (Avastin®) Treatment For Wet Age-related Macular Degeneration (AMD). *Proc ARVO (Assoc for Research in Vision and Ophthalmology) Annual Meeting* Fort Lauderdale (USA), May 2011.

[52] J. Ding, M.W Strachan, R.M Reynolds, et al. Diabetic retinopathy and cognitive decline in older people with type 2 diabetes: the Edinburgh Type 2 Diabetes Study. *Diabetes* 59(11), 2883-9, 2010.

[53] F.N Doubal, T.J MacGillivray, N. Patton, et al. Fractal analysis of retinal vessels suggests that a distinct vasculopathy causes lacunar stroke. *Neurology* 74(14), 1102-1107, 2010.

[54] F. Doubal, P. Hokke, J. Wardlaw. Retinal microvascular abnormalities and stroke - a systematic review. *J. Neurol. Neurosurg. Psychiatry*, vol. 80, no. 2, pp. 158 165, 2009.

[55] F. Doubal, B. Dhillon, M. S. Dennis, and J. M. Wardlaw, Retinopathy in ischemic stroke subtypes. *Stroke*, vol. 40,no. 2, pp. 389 393, 2009.

[56] F. N. Doubal, T. J.MacGillivray, P. E. Hokke, B. Dhillon, M. S. Dennis, J. M. Wardlaw. Differences in retinal vessels support a distinct vasculopathy causing lacunar stroke. *Neurology*, vol. 72, pp. 1773 1778, 2009.

[57] J. Ding, N. Patton, I. J. Deary, M. W. Strachan, F. G. Fowkes, R. J. Mitchell, J. F. Price. Retinal microvascular abnormalities and cognitive dysfunction: a systematic review. *Brit. J. Ophth*, vol. 92, no. 8, pp. 1017 1025, 2008.

[58] N. Patton, T. M. Aslam, T. J. MacGillivray, I. J. Deary, B. Dhillon, R. H. Eikelboom, K. Yogesan, I. J. Constable. Retinal image analysis: concepts, applications and potential. *Prog. Retin. Eye Res*, vol.25, no. 1, pp. 99 127, 2006.

[59] N. Patton, T. Aslam, T. J. MacGillivray, A. Pattie, I. J. Deary, B. Dhillon. Retinal vascular image analysis as a potential screening tool for cerebrovascular disease. *Journal of Anatomy*, vol. 206, pp. 318 348, 2005.

[60] J. S.Wolffsohn, G. A. Napper, S-M. Ho, A. Jaworski, T. L. Pollard. Improving the description of the retinal vasculature and patient history taking for monitoring systemic hypertension. *Ophthalmic and Physiological Optics*, vol. 21, no. 6, pp. 441 449, 2002.

[61] N.Patton, A.Pattie, T.MacGillivray, T.Aslam, B.Dhillon, A.Gow, J.M. Starr, L.J. Whalley, I.J. Deary. The Association between Retinal Vascular Network Geometry and Cognitive Ability in an Elderly Population. *Investigative Ophthalmology & Visual Science*, Vol. 48, No. 5, May 2007.

[62] R.M Gunn.On ophthalmoscopic evidence of general arterial disease. *Trans Ophthalmol Soc UK* 18:356–81, 1898.

[63] R.M Gunn.Opthalmocsopic evidence of (1) arterial changes associated with chronic renal diseases and (2) of increased arterial tension. *Trans Ophthalmol Soc UK* 12:124–5, 1892.

[64] T.Mo, LM Jampol. Pathophysiology of hypertensive retinopathy. *Ophthalmology* 89:1132–45, 1982.

[65] T.Mom, Abrams GW, Jampol LM. Hypertensive retinopathy, choroidopathy, and optic neuropathy: a clinical and pathophysiological approach to classification, in Singerman LJ, Jampol LM (eds): Retinal and Choroidal Manifestations of Systemic Disease. *Baltimore, Williams and Wilkins*, pp 79–127, 1991.

[66] R.E.Wells, M.Herman, R.Gorlin. Microvascular changes in coronary artery disease. *Circulation* 33–34:237, 1966.

[67] J.P.Wendland. Retinal arteriolosclerosis in age, essential hypertension, and diabetes mellitus. *Trans Am Ophthalmol Soc* 64:735–61, 1966.

[68] N.M Keith, H.P Wagener, N.W Barker. Some different types of essential hypertension: their course and prognosis. *Am J Med Sci* 197:332–43, 1939.

[69] S.B Dimmitt, J.N West, S.M Eames, et al. Usefulness of ophthalmoscopy in mild to moderate hypertension. *Lancet* 1:1103–6, 1989.

[70] P.M Dodson, G.Y Lip, S.M Eames, et al. Hypertensive retinopathy:a review of existing classification systems and a suggestion for a simplified grading system. *J Hum Hypertens* 10:93–8, 1996.

[71] A.Kagan, E.Aurell, J.Dobree. A note of signs in the fundus oculi and arterial hypertension: conventional assessment and significance. *Bull World Health Organ* 34:955–60,1966.

[72] H.D Schubert. Ocular manifestations of systemic hypertension. *Curr Opin Ophthalmol* 9:69–72, 1998.

[73] J.B Walsh. Hypertensive retinopathy. Description, classification, and prognosis. *Ophthalmology* 89:1127–31, 1982.

[74] N. Patton, T.M. Aslam, T. MacGillivray et al. Retinal image analsyis: Concepts, applications and potential. *Progress in Retinal and Eye Research* 25:99-127, 2006.

[75] L.Hubbard, B.Ehrhardt, R.Klein. The association between generalized arteriolar narrowing and blood pressure. *Invest. Ophthalmol*. Vis. Sci. 33 (Suppl.),804, 1992.

[76] H.Leung, J.Wang, E. Rochtchina, A.Tan, T.Wong, L.Hubbard, P.Mitchell. Computer-assisted retinal vessel measurement in an older population: correlation between right and left eyes. *Clin. Exp. Ophthalmol*. 31,326–330, 2003.

[77] T.Wong, M.Knudtson, R.Klein, B.Klein, S.Meuer, L.Hubbard. Computer-assisted measurements of retinal vessel diameters in the Beaver Dam Eye Study—methodology,correlation between eyes and effect of refractive errors. *Ophthalmology* 111,1183–1190, 2004.

[78] T.Y.Wong, A.Shankar, R.Klein, B. E. K. Klein, L.D. Hubbard. Retinal Arteriolar Narrowing, Hypertension, and Subsequent Risk of Diabetes Mellitus. *Archives of Internal Medicine*. 165:1060-1065; 2005.

[79] T.Y.Wong, R. Klein, A.R. Sharrett et al. Retinal Arteriolar Narrowing and Risk of Coronary Heart Disease in Mean and Women: The Atherosclerosis Risk in Communities Study. *Journal of the American Medical Association*. 287:1153-1159; 2002.

[80] T.Y.Wong, R. Klein, A.R. Sharrett et al. Retinal Arteriolar Narrowing and Risk of Diabetes Mellitus in Middle-aged Persons. *Journal of the American Medical Association*. 287:2528-2533; 2002.

[81] T.Wong, B.Duncan, S.Golden, R.Klein, D.Couper, B. Klein, L.Hubbard, A.Sharrett, M.Schmidt. Associations between the metabolic syndrome and retinal microvascular signs: the Atherosclerosis Risk in Communities Study. *Invest. Ophthalmol.Vis. Sci.* 45,2949–29 54, 2004.

[82] R.Klein, A,Sharrett, B.Klein, L.Chambles, L.Cooper, L.Hubbard, G.Evans. Are retinal arteriolar abnormalities related to atherosclerosis? The Atherosclerosis Risk in Communities Study. *Arterioscler. Thromb. Vasc. Biol*. 20,1644–16 50, 2000.

[83] T.Wong, J.Wang, E.Rochtchina, R.Klein, P.Mitchell. Does refractive error influence the association of blood pressure and retinal vessel diameters? The Blue Mountains Eye Study. *Am.J. Ophthalmol*. 137,1050–1055, 2004.

[84] J.Wang, P.Mitchell, H.Leung, E.Rochtchina, T.Wong, R.Klein. Hypertensive retinal vessel wall signs in a general older population: the Blue Mountains Eye Study. *Hypertension* 42, 534–541, 2003.

[85] K.Lee, B.Klein, R.Klein, M.Knudston. Familial aggregation of retinal vessel caliber in the Beaver Dam Eye Study. *Invest. Ophthalmol. Vis. Sci*, 2004.

[86] R. Klein, B. Klein,S. Tommy, T. Wong. The relation of retinal microvascular characteristics to age-related eye disease: the Beaver Dam eye study. *Am. J. Ophthalmol*. 137,435–444, 2004.

[87] University of Michigan Kelogg Eye Centre
http://www.kellogg.umich.edu/theeyeshaveit/optic-fundus/images/disc-pallor.jpg

[88] J.W.Chan "Congenital Disc Anomalies" *Springer Link, Book chapter Optic Nerve Disorders*. 201-219, 2007.

[89] Y.Zheng, T.Y. Wong, C.Y.L.Cheung, E. Lamoureux, P. Mitchell, M. He, T.Aung Influence of Diabetes and Diabetic Retinopathy on the Performance of Heidelberg Retina Tomography II for Diagnosis of Glaucoma. *Investigative Ophthalmology & Visual Science*, Vol. 51, No. 11, 2010.

[90] A. Hoover, V. Kouznetsova, and M. Goldbaum. Locating blood vessels in retinal images by piecewise threshold probing of a matched fillter response. *IEEE Transactions on Medical Imaging*, 19(3):203210, 2000.

[91] J. Staal, M. D. Abramo_, M. Niemeijer, M. A. Viergever, and B. van Ginneken. Ridge-based vessel segmentation in color images of the retina. *IEEE Transactions on Medical Imaging*, 23(4):501,509, 2004.

[92] The Oeil project
http://www.lesia.obspm.fr/astro/optada/OEIL/images/Scan_OCT.jpg

[93] D.J Couper, R. Klein, L.D. Hubbard, T.Y Wong, P.D Sorlie, L.S Cooper, R.J Brothers, F.J Nieto. Reliability of retinal photography in the assessment of retinal microvascular characteristics: the Atherosclerosis Risk in Communities study. *Am J Ophthalmol* 133:78–88, 2002.

[94] D.K.Wallace, S.Freedman, Z.Zhao. S.H.Jung. Accuracy of ROPtool vs Individual Examiners in Assessing Retinal Vascular Tortuosity. *Arch Ophthalmol*, Vpl. 125(no.11) Nov 2007.

[95] T. Aslam, B. Fleck, N. Patton, E. Trucco, H. Azegrouz. Digital image analysis of plus disease in retinopathy of prematurity. *Acta Ophthalmologica*. 87:368-377, 2009.

[96] C.G. Owen, A.R. Rudnicka, R. Mullen, S.A. Barman, D. Monekosso et al. Measuring Retinal Vessel Tortuosity in 10-year-old Children: Validation of the Computer-assisted Image Analysis of the Retina (CAIAR) Program. *IOVS*, Vol.50, No.5, May 2009.

[97] A.D. Fleming, S. Philip, K.A. Goatman, J.A. Olson, P.F. Sharp. Automated Assessment of Diabetic Retinal Image Quality Bsed on Clarity and Field Definition. *IOVS*. Vol.47, No.3, March 2006.

[98] C.M. Wilson, K.D. Cocker, M.J. Moseley, C. Paterson et al. Computerized Analysis of Retinal Vessel Width and Tortuosity in Premature Infants. *IOVS*. Vol.49, No.8, August 2008.

[99] M.F. Chiang, P.J. Thyparampil, D.Rabinowitz. Interexpert Agreement in the Identification of Macular Location in Infants at Risk for Retinopathy of Prematurity. *Arch Ophthalmol*, 128(9):1153-1159. 2010.

[100] E. Trucco, H. Azegrouz, and B. Dhillon. Modeling the tortuosity of retinal vessels: does calibre play a role? *IEEE Transactions on Biomedical Engineering*, 57(9):2239,2247, 2010.

[101] C.L.Tsai, C.V. Stewart, H.L.Tanenbaum, B. Roysam. Model-Based Method for Improving the Accuracy and Repeatability of Estimating Vascular Bifurcations and Crossovers From Retinal Fundus Images. *IEEE transactions on Information Technology in Biomedicine*. vol.8, no.2, 2004.

[102] R.Chrastek, M. Wolf, K. Donath, H. Niemann. Automated calculation of retinal arteriovenous ratio for detection and monitoring cerebrovascular disease based on assessment of morphological changes of retinal vascular system. *IAPR Owrkshop on Machine Vision Applications*, Dec, 11-13, 2002.

[103] S. G. Vázquez, N. Barreira, M. G. Penedo, M. Ortega, A. Pose-Reino. Improvements in retinal vessel clustering techniques: towards the automatic computation of the arterio venous ratio. *Computing* 90:197–217. 2010

[104] H.M. Pakter, E. Ferlin, S.C. Fuchs, et al. Measuring arteriolar-to-venous ratio in retinal photography of patients with hypertension: Development and application of a new semi-automated method. *American Journal of Hypertension*, 18:417-421; 2005.

[105] H. Li, W. Hsu, M.L. Lee, T.Y Wong. Automatic Grading of Retinal Vessel Caliber. *IEEE Transactions in Biomedical Engineering*. Vol. 52, No.7, July 2005.

[106] A. Ruggeri, E. Grisan, and M. De Luca. An automatic system for the estimation of generalized arteriolar narrowing in retinal images. *Proc. 29th Annual International Conference of the IEEE Engineering in Medicine and Biology Society EMBS*, pp. 6463–6466, 2007.

[107] Z. Guo and R. W. Hall. Parallel thinning with two-subiteration algorithms. *Communications of the ACM*, 32:359,373, 1989.

[108] L.Giancardo, F. Meriaudeau, T.P. Karnowski, Y. Li, S.Garg, K.W. Tobin Jr.,E.Chaum. Exudate-based diabetic macular edema detection in fundus images using publicly available datasets. *Medical Image Analysis* 16, 216–226, 2012.

[109] AM Mansour. Racial Variation of Optic Disc Size. *Ophthalmic Res*, 23:67–72, 1991.

[110] M.I.Seider, R.Y Lee, D.Wang, M.Pekmezci, T.C. Porco, S.C Lin. Optic Disk Size Variability Between African, Asian, Caucasian, Hispanic and Filipino Americans Using Heidelberg Retinal Tomography. *J Glaucoma*. 18(8): 595–600, 2009.